Numerical Investigation into Size Effect

on Prestressed Concrete Beam Resistance to Shear Tension Cracking

A. Sugianto
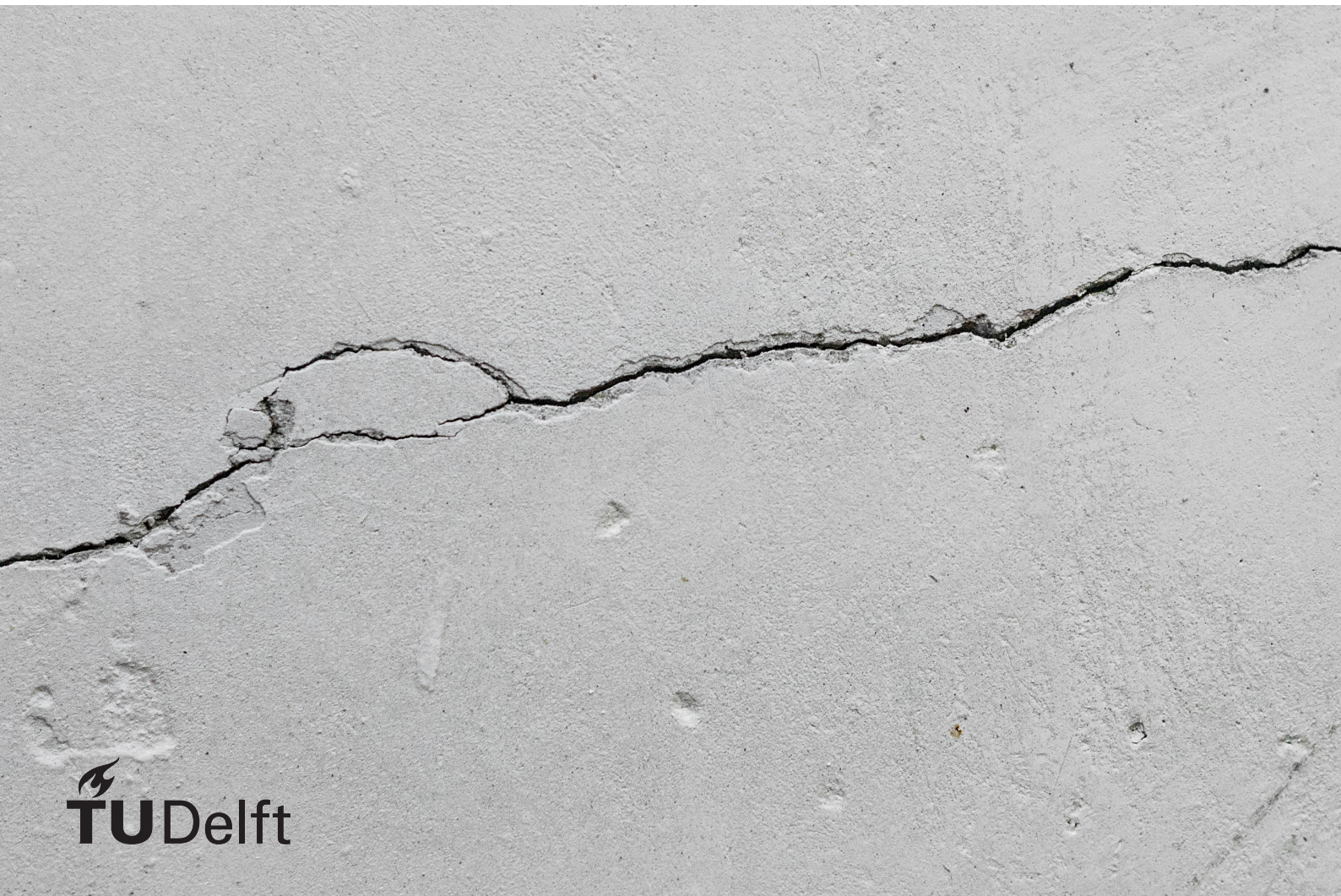
Numerical Investigation into Size Effect

on Prestressed Concrete Beam
Resistance to Shear Tension Cracking

by

A. Sugianto

in partial fulfillment of the requirements for the degree of

Master of Science
in Structural Engineering

at the Delft University of Technology

Student number:	4666836	
Committee Members:	Dr. ir. M. A. N. Hendriks	TU Delft, supervisor
	Dr. ir. C. van der Veen	TU Delft
	Ir. M. A. Roosen	TU Delft

TUDelft

Preface

This thesis was written as part of an assignment for Additional Graduation Work (CIE5050-09) course. It was finalized as a partial fulfillment in obtaining the degree of Master of Science in Structural Engineering at Delft University of Technology. Besides that, the author also wrote this thesis in the hope of giving a meaningful contribution towards the civil engineering community in understanding the size effect in shear tension cracking even further.

This thesis would not have finished without the support of the author's supervisor and committee members. I would like to thank Dr. ir. M. A. N. Hendriks for being supportive with his vast knowledge and patient in taking my numerous questions, Dr. ir. C. van der Veen for helping me to understand more about concrete through hours of consultations and, Ir. M. A. Roosen for a lot of his time, patience, and guidance for me in finishing the thesis. I would also like to thank all my friends who helped me get through tough times in understanding the size effect, DIANA FEA, and LaTeX.

<div align="right">

Andrew Sugianto
Delft, January 2019

</div>

Abstract

In the past, many research on the topic of size effect on concrete structures were mainly focused on the phenomenon of size effect in flexural cracking. The result of those studies can be found today in the concrete structure design specifications of well-known building codes, such as the Eurocode. Nevertheless, the inclusions of the results of those studies into the design specifications are still minimum and therefore, it is necessary to conduct more studies on size effect, especially on other types of cracking.

In this thesis, an investigation focused on the size effect in shear tension cracking at prestressed concrete beams was conducted. The model used for investigating the size effect is a prediction that a shear tension crack will occur when the principal tensile stress at a certain location on the web of a beam is equal to the concrete mean uniaxial tensile strength $\left(\sigma_1 = f_{ctm} \right)$. The investigation was conducted by studying premature shear tension cracking on a group of several I-profile prestressed reinforced concrete beams, called the trusted specimens, which were experimented by Hanson (1964), Choulli (2005), and Elzanaty (1986) under four-point bending tests. These tested beams were numerically investigated using linear elastic finite element analysis (LEFEA) with an aim to find the nearly realistic principal tensile stresses that caused the shear tension crack to initiate below the designated tensile strength of the beams.

To study the size effect, the obtained principal tensile stress distributions were analyzed using two new approaches proposed by the author, namely the σ_1 area approach and the ratio-of-distances approach. The σ_1 area method is a technique for detecting a structural size dependency of the uniaxial tensile strength by comparing rectangles which areas represents a group of σ_1 values that have a higher likelihood in achieving the deviated values of f_{ctm} and initiate shear tension cracking on the web of the trusted specimens. In contrast, the ratio-of-distances approach investigates the size dependency of the uniaxial tensile strength by observing the locations of σ_{1max} where a shear tension crack initiated in the web of each trusted specimen under an assumption that a shear tension crack is more likely to originate from near the beam neutral axis instead of near the web-flange junction due to the change of thickness at that interface.

In conclusion, the result of the investigation was presented. The σ_1 area approach confirmed the presence of size effect in shear tension cracking at the trusted specimens by giving a relation that showed a tendency for the smaller specimens to have a higher resistance towards principal tensile stresses compared to the larger specimens. The ratio-of-distances result, on the other hand, implied that the approach has failed to detect the presence of size effect. In that result, the shear cracks from the smaller specimens and the shear cracks from the larger specimens had similar starting points locations, at which the σ_{1max} was located.

In addition, several recommendations are provided for future studies on size effect in shear tension cracking. It was recommended to do research this topic on different physical problems and shear tension cracking with the presence of flexural cracks.

Contents

1

Introduction

In today's engineering practice, engineers are well aware that life-size structures, especially the ones that were made of quasi-brittle material such as concrete, tend to fail prematurely at a stress level that is lower than the structure's designated strength. This phenomenon is commonly known as the size effect. The size effect occurs because the material used to build a life-size structure has more strength deviation when compared with the same material used in an experimental-size structure due to material strength randomness. The discovery of the size dependency of nominal strengths of structure contradicts the assumption of classical theories of elasticity and plasticity in which it is stated that a nominal strength is size independent.

In the past, numerous studies on the topic of size effect on concrete structures were conducted with an aim to prevent the occurrence of premature cracks on structural members. Many of those studies were mainly focused on the phenomenon of size effect in flexural cracking and the result of those studies can be found today in the concrete structure design specifications of well-known building codes, such as the Eurocode. In the Eurocode, the inclusions of size effect can be recognized in expression 3.23 for defining the concrete flexural strength $\left(f_{ctm,fl}\right)$ and expression 6.2.a for defining the shear resistance $\left(V_{Rd,c}\right)$ in members that do not require shear reinforcement. Nevertheless, the inclusions of the results of those studies into the design specifications are still minimum and therefore, it is necessary to conduct more studies on size effect, especially on other types of cracking.

In the Netherlands, the studies on size effect can be related to the recent reassessment process on the strength of dated concrete structures around the country performed by its government. In this on-going reassessment process, the government is working with their engineers to do evaluations on those structures that include premature crack occurrence as one of the evaluation points. The goal of this evaluation is to know if the old structures can still be safely used for another several decade before there is a necessity for them to be replaced. The knowledge about the size effect comes as a basis for the engineers to gain the actual nominal strength of the structures and to help them determine the additional service lifetime of those aged structures.

As an addition to the studies on the size dependency of structural strengths, the author presented this thesis which was aimed to answer the following research questions:

1. *Is there any presence of size effect regarding the resistance of prestressed concrete beams on shear tension cracking?*

2. *Is the resistance of the shear tension crack at the web-flange junction higher than anywhere in the web?*

The research for this thesis was focused on the size effect in shear tension cracking on prestressed concrete beams. The model used for investigating the size effect is a prediction that a shear tension crack will occur when the principal tensile stress at a certain location on the web of a beam is equal to the concrete mean uniaxial tensile strength $\left(\sigma_1 = f_{ctm}\right)$. The subjects of this research were I-profile prestressed concrete beams which were tested by Hanson (1964), Choulli (2005), and Elzanaty (1986) under four-point flexural tests. The beams were then numerically investigated using linear elastic finite element analysis (LEFEA) with

a goal to find the true principal tensile stress distribution in the beams at the occurrence of the shear tension crack.

Then, two new approaches proposed by the author were used to observe the principal tensile stress distributions to detect the presence of the size effect. They are the σ_1 area approach and the ratio-of-distances approach. These approaches are essential for this numerical investigation since the research only involved experimental-size beams and there was no established approach yet for studying the size effect in shear tension cracking when the author started this study. These approaches were created to help the author to find an explanation that can describe the influence of structural size to the deviation of the uniaxial tensile strength in an I-profile prestressed concrete beam.

2

Literature Review

2.1. Stress

In continuum mechanics, stress is known as the intensity of internal forces inside a material body in equilibrium, as shown in Figure 2.1, that is continuously distributed over a specific cross-sectional area of the body while the body itself is loaded with external forces [9]. The magnitude of stress is defined by the amount of resultant force per unit area of the surface on which they act.
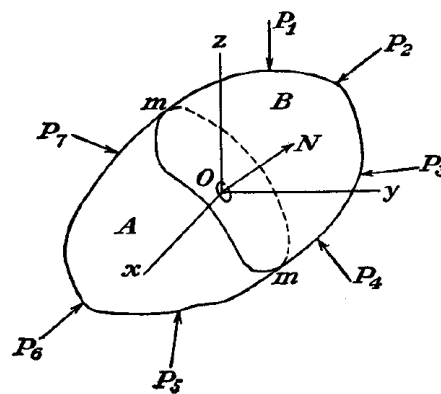
Figure 2.1: A Material Body in Equilibrium [11]

2.1.1. Normal Stress and Shear Stress

Based on its direction on a plane, stress can be divided into two types of stress components: normal stress and shear stress. Normal stress is defined as stress that acts in the direction normal to a plane and conversely, stresses that act in the direction parallel to a plane is called shear stress. In many references, a normal stress component can be denoted by a σ followed with one or two repeated subscript indexes. For a shear stress component, it can be denoted by τ or σ followed with two different subscript indexes. The first index indicates the plane at which stress acts on and the second index indicates the direction of stress. For instance, normal stress working in the direction of x-axis and on an x-plane will be denoted as σ_x or σ_{xx} and shear stress acting on the x-plane in the direction of y-axis will be indicated as σ_{xy} or τ_{xy}.

In a 3D Cartesian coordinate system, each plane parallel to a coordinate axis can have three positive components of stress: one normal stress component and two shear stress components, as presented in Figure 2.2. The positive direction of these components depends on the coordinate direction they coincide with. For example, on a positive x-plane, a stress component is positive when it acts in the positive coordinate direction and, conversely, on a negative x-plane, a stress component is positive when it works in the negative coordinate direction. Based on these sign convention descriptions, the positive direction of the stress components

acting of the six sides of a cubic element, that represents a point in a body, can have a definition indicated in Figure 2.3.
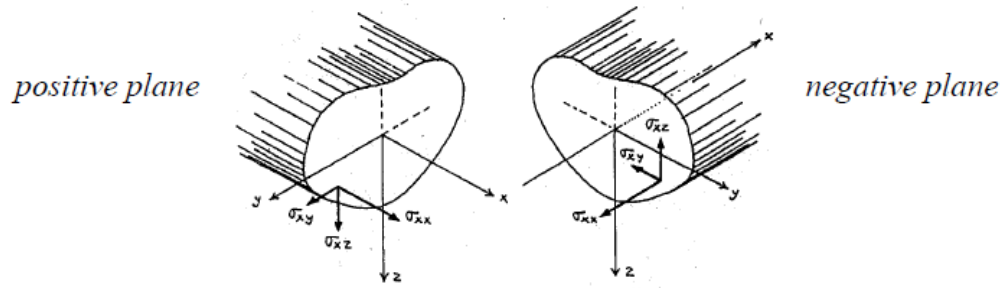
Figure 2.2: Normal Stress and Shear Stress in Positive and Negative Planes [11]
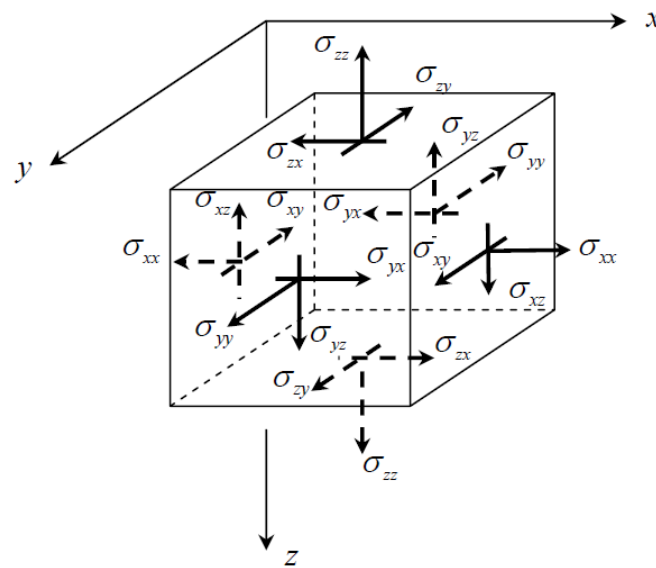
Figure 2.3: Positive Directions of Stress Components on A Cubic Element [11]

Despite having different positive directions, the normal stresses and the shear stresses on each pair of parallel sides of a cubic element are similar in magnitude. As a result, these stress components can be placed into groups according to the plane they are located on:

- On x-plane: σ_{xx}, σ_{xy}, and σ_{xz}

- On y-plane: σ_{yx}, σ_{yy}, and σ_{yz}

- On z-plane: σ_{yx}, σ_{yy}, and σ_{yz}

In tensor form, these nine stress components can be presented as a 3 x 3 second-order tensor known as the Cauchy stress tensor. This stress tensor is often used in stress analysis on material bodies under the assumption of small deformations. This tensor is a symmetrical tensor by having $\sigma_{xy} = \sigma_{yx}$, $\sigma_{xz} = \sigma_{zx}$, and $\sigma_{yz} = \sigma_{zy}$, which means that the general stress state of a point inside a body can be characterized by only six independent normal and shear stress components instead of nine. Following all those descriptions, the Cauchy stress tensor can be expressed as follows:

$$\sigma = \begin{bmatrix} \sigma_{xx} & \sigma_{xy} & \sigma_{xz} \\ \sigma_{yx} & \sigma_{yy} & \sigma_{yz} \\ \sigma_{zx} & \sigma_{zy} & \sigma_{zz} \end{bmatrix} \tag{2.1}$$

In a condition where an element solely experiences a moment, its normal stress component that acted in the x-axis direction can be computed analytically using the following expression[7]:

$$\sigma_{xx} = \frac{M \, y \, E(y)}{\int y^2 \, E(y) \, dA} \tag{2.2}$$

On the other hand, if there are only axial forces acting of an element, the following formula can be used to define its normal stress component in the x-axis direction[7]:

$$\sigma_{xx} = \frac{F}{A} \tag{2.3}$$

In case of the shear stress component, it can be calculated analytically using the following formula[7]:

$$\tau_{xy} = \frac{V \int y \, E(y) \, dA}{t \int y^2 \, E(y) \, dA} \tag{2.4}$$

where:

M internal bending moment

y a certain distance in the y-axis direction from the beam neutral axis

E modulus of elasticity

F axial forces acting on the surface of a cross-section

A element cross-sectional area

V internal shear force

t thickness of the element

2.1.2. Plane Stress Situation

In a certain condition, a material body can have a situation in which all stress components on one of its plane are equal to zero and it is known as the plane stress situation. Plane stress situation on a y-plane causes the stress at a point to be described only by σ_x, σ_y,and τ_{xy} which act on four faces of the cubic element, while the stress components working on the faces parallel to the y-plane are equal to zero ($\sigma_z = \tau_{xz} = \tau_{yz} = 0$), as presented in Figure 2.5. In other words, the plane stress causes the stress components to become independent of y.
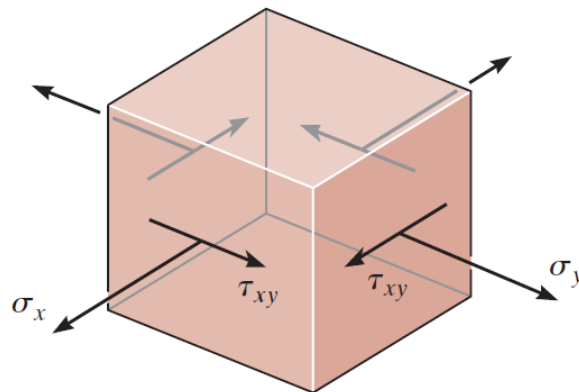
Figure 2.4: Plane Stress Situation [7]

Plane stress situation is frequently used in engineering practice, especially in analyzing a beam. The classical beam theories, such as Euler-Bernoulli beam theory, made the simplification of on the load modeling on a beam so that the stress produced in a structural member can be analyzed in a single plane, which, in this case, is the vertical cross section of a beam. Due to that, the normal and shear stresses are assumed to be distributed over the depth of a beam. Also, if a very small specimen of a beam at a distance z from the neutral axis is considered, it is safe to assume that the stresses on that specimen are uniform.
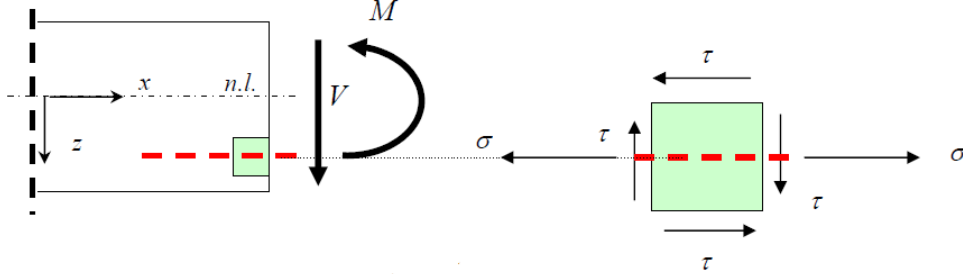
Figure 2.5: Plane Stress Situation Applied in Beam Analysis [11]

2.1.3. Principal Stress

Principal stress is a stress condition at which normal stress component reaches an extreme value while its shear counterpart has a value of zero. Normally, principal stresses are distinguished into two types of stress: the maximum principal stress and the minimum principal stress which are often denoted as σ_1 and σ_2, respectively. Nevertheless, in common engineering practice, σ_1 is often used to represent the principal tensile stress and σ_2 is to represent the principal compressive stress. In a condition where the minimum principal stress is less than zero and the maximum principal stress is zero or negative, a cubic element will experience a pure compressive state, and in a complete opposite state, that same element will experience a pure tensile state. Moreover, since principal stress is a vector, its direction is often referred to as the trajectory.

One way of obtaining in-plane principal stress value of a plane stress element is by doing stress transformation. Through the transformation, the x-y Cartesian coordinate system used to define global normal and shear stresses of an element will be rotated as much as θ into an x'-y' coordinate system at which new normal and shear stress components can be acquired. Furthermore, to get the principal stress values, θ has to reach a certain angle at which the normal stresses can yield maximum value.

An expression that defines the principal stress value can be obtained through several mathematical derivations. As a starting point, a plane stress element is cut along an arbitrary inclined plane and one part of its segments is separated, as shown in Figure 2.6. If the area of the segment is assumed to be ΔA, the area of the horizontal and vertical faces of the separated segment is $\Delta A \sin\theta$ and $\Delta A \cos\theta$, respectively. The free-body diagram of the segment can be seen in Figure 2.6(b).

Then, the unknown normal and shear stress components, $\sigma_{x'}$ and $\tau_{x'y'}$ which were generated at the new x'-y' coordinate system can be determined using the force equilibrium equation:

$$\Sigma F_{x'} = 0; \ \sigma_{x'} = \sigma_x \cos^2\theta = \sigma_y \sin^2\theta + \tau_{xy}(2\sin\theta\cos\theta) \tag{2.5}$$

$$\Sigma F_{y'} = 0; \ \tau_{x'y'} = (\sigma_y - \sigma_x)\sin\theta\cos\theta + \tau_{xy}(\cos^2\theta - \sin^2\theta) \tag{2.6}$$

Using trigonometric identities $\sin 2\theta = 2\sin\theta\cos\theta$, $\sin^2\theta = (1-\cos 2\theta)/2$, and $\cos^2\theta = (1+\cos 2\theta)/2$, Equation 2.5 and 2.6 can be simplified into:

$$\sigma_{x'} = \frac{\sigma_x + \sigma_y}{2} + \frac{\sigma_x - \sigma_y}{2}\cos 2\theta + \tau_{xy}\sin 2\theta \tag{2.7}$$

$$\sigma_{y'} = \frac{\sigma_x + \sigma_y}{2} - \frac{\sigma_x - \sigma_y}{2}\cos 2\theta - \tau_{xy}\sin 2\theta \tag{2.8}$$
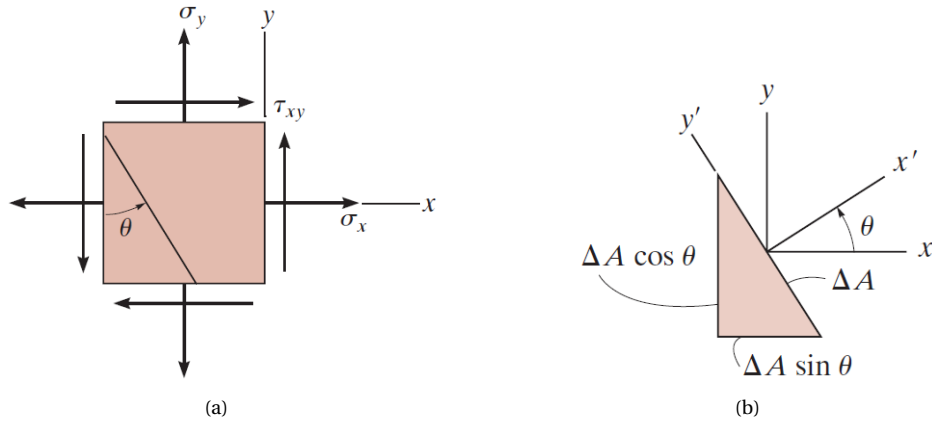
Figure 2.6: (a) Plane Stress Element with A Cut (b) Segment of The Cut Plane
Stress Element [7]

$$\tau_{x'y'} = -\frac{\sigma_x - \sigma_y}{2}\sin 2\theta + \tau_{xy}\cos 2\theta \tag{2.9}$$

After Equation 2.7, 2.8, and 2.9 are acquired, stress transformation can be applied by substituting the known values of σ_x, σ_y, τ_{xy}, and θ in accordance with the given sign convention. It is apparent from these equations that the magnitude of σ_x, σ_y, and $\tau_{x'y'}$ have a dependency on the orientation of the plane stress element which is represented by θ. To obtain the value of the principal stresses, a certain inclination angle has to be determined in order for the normal stresses to be able to produce their maximum and minimum value and that angle $\theta = \theta_p$ can be calculated using the following equation:

$$\frac{d\sigma_{x'}}{d\theta} = -\frac{\sigma_x - \sigma_y}{2}(2\sin 2\theta) + 2\tau_{xy}\cos 2\theta = 0 \tag{2.10}$$

which can be solved into:

$$\tan 2\theta_p = \frac{\tau_{xy}}{(\sigma_x - \sigma_y)/2} \tag{2.11}$$

Solving Equation 2.11 gives us θ_{p1} and θ_{p2} that describe the direction of maximum and minimum normal stress. Specifically, the values of $2\theta_{p1}$ and $2\theta_{p2}$ should be 180° apart. Substituting θ_{p1} and θ_{p2} into Equation 2.7 gives:

$$\sigma_{1,2} = \frac{\sigma_x + \sigma_y}{2} \pm \sqrt{\left(\frac{\sigma_x - \sigma_y}{2}\right)^2 + \tau_{xy}^2} \tag{2.12}$$

In addition, substituting θ_{p1} and θ_{p2} into Equation 2.9 yields $\tau_{x'y'} = 0$. This means that at this orientation, the plane stress element does not experience any shear stresses and θ_{p1} and θ_{p2} have indeed produced the principal stresses.

2.2. Shear Tension Crack

Shear tension crack, which also known as diagonal tension crack, is an inclined crack that occurs from an interior point in the web of a concrete beam due to the principal tensile stress reaches the tensile strength of the beam in an area which is uncracked by the flexural stress. The diagonal crack, as shown in Figure 2.7 together with other common types of cracks, generally form normal to the direction of the principal tensile stress and more likely to occur on prestressed concrete beams than on reinforced concrete beam. In an ultimate limit state, a shear tension crack can cause a diagonal tension failure to a concrete beam with an amount of stirrups that is lower than its minimum requirement.
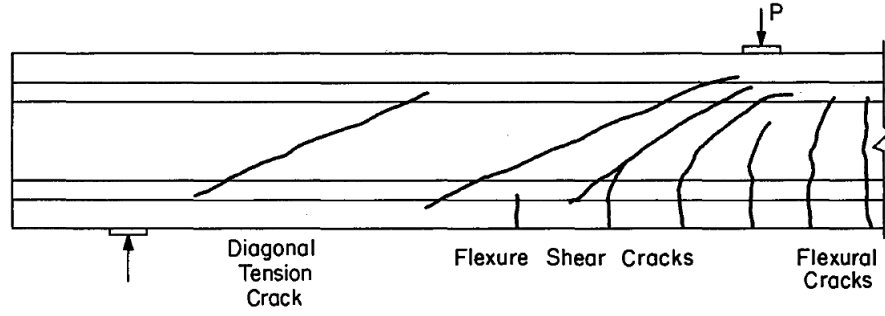
Figure 2.7: Diagonal Tension Crack Compared with Other Types of Cracks [6]

By neglecting the small contribution of the normal stress component to the y-direction (σ_{yy}) in the Bernoulli region to the overall stress, the principal tensile stress in the web can be calculated using the Mohr's circle in Figure 2.8(b) which produced a simpler mathematical expression [10] than Equation 2.12, as shown below:

$$\sigma_1 = \frac{\sigma_N}{2} + \sqrt{\left(\tau^2 + \frac{\sigma_N^2}{4}\right)} \tag{2.13}$$

(a)   (b)
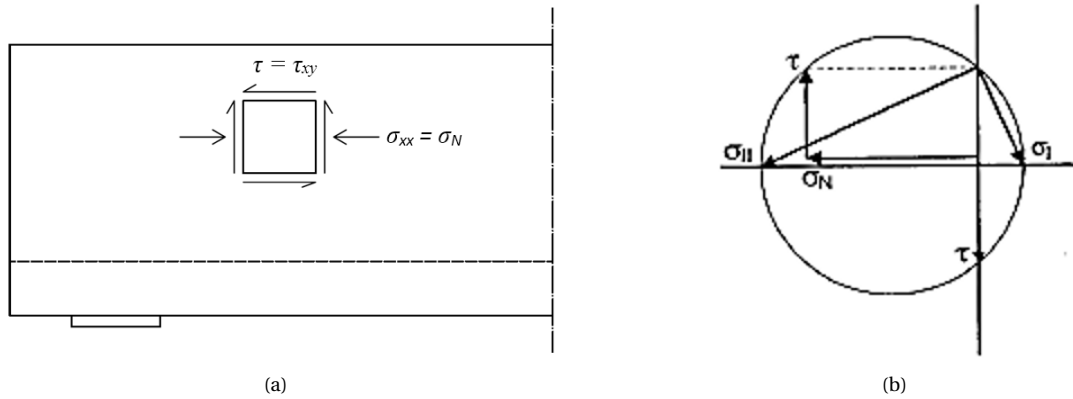
Figure 2.8: Calculation of Shear Tension Capacity with Mohr's Circle [10]

After obtaining the σ_1 value, the capacity of the beam to resist shear tension crack can be calculated. By substituting $\tau = V_{Rd,ct}\, S / b_w\, I$ and $\sigma_N = \alpha_l\, \sigma_{cp}$ into Equation 2.13, an expression for shear tension capacity, as written in equation 6.4 of Eurocode 2 EN 1992-1-1:2004 [1], is obtained:

$$V_{Rd,ct} = \frac{I\, b_w}{S} \sqrt{\left(f_{ctd}\right)^2 - \alpha_l\, \sigma_{cp}\, f_{ctd}} \tag{2.14}$$

where:

I the second moment of area

b_w the width of the cross section at the centroidal axis

S the first moment of area above and about the centroidal axis

α_l $= l_x / l_{pt2} \leq 1.0$ for pretensioned tendons

       $= 1.0$ for other types of prestressing

l_x the distance of section considered from the starting point of the transmission length

l_{pt2} the upper bound value of the transmission length of the prestressing element

σ_{cp} the concrete compressive stress at the centroidal axis due axial loading and/or prestressing

Since this formula is used in an experimental fashion for this study, the mean uniaxial tensile strength $\left(f_{ctm}\right)$ is used instead of the design tensile strength $\left(f_{ctd}\right)$ and σ_{cp} is assumed to be equal to σ_{xx}. Thus, Equation 2.14 changes into:

$$V_{cr} = \frac{I\, b_w}{S} \sqrt{\left(f_{ctm}\right)^2 - \alpha_l\, \sigma_{xx}\, f_{ctm}}$$

               (2.15)

2.3. Uniaxial Tensile Strength

In common engineering practice, uniaxial tensile strength is generally used to define a concrete structure capacity in resisting tension. Since it is difficult to test a concrete sample in pure axial tension, its value is often determined from indirect tests at which certain parameters can be measured, such as the modulus of rupture which comes from a bending test, the splitting strength which is produced by splitting a concrete cylinder with a line load, or concrete compressive strength from a compression test on concrete cylinder. In an axial tension experiment, a concrete sample usually shows a strain-stress response that is nearly linear until it reaches its cracking phase.

2.3.1. Based on Eurocode

In the Eurocode, the uniaxial tensile strength is derived from the value of concrete compressive strength. According to table 3.1 in Eurocode 2 1992-1-1:2004 [1], the mean uniaxial tensile strength $\left(f_{ctm}\right)$ of a concrete that has a f_{ck} value above C50/60 can be determined using the following equation:

$$f_{ctm} = 2.12\, ln\left(1 + \frac{f_{cm}}{10}\right)$$

               (2.16)

and for a concrete structure that has a f_{ck} value equal to or below C50/60, the f_{ctm} can be defined with the following formula [1]:

$$f_{ctm} = 0.3\left(f_{ck}\right)^{\frac{2}{3}}$$

               (2.17)

where:

f_{ck} characteristic cylinder strength (5%)

f_{cm} mean compressive strength at 28 days

In addition, based on table 3.1, f_{cm} can be found using the following relation [1]:

$$f_{cm} = f_{ck} + 8\ N/mm^2$$

               (2.18)

But, because experimental samples usually have better quality control and thus, fewer strength deviations, Equation 2.18 can be replaced with the following relation:

$$f_{cm} = f_{ck} + 4\ N/mm^2$$

               (2.19)

2.3.2. Based on ACI

In determining the uniaxial tensile strength, American Concrete Institute (ACI) took the size effect into the consideration. It is based on the fact that the uniaxial tensile stress (or the cracking stress) tends to decrease when a volume of concrete subjected to high tensile stress is increased. Hence, larger concrete structural members tends to crack at a lower tensile stress than at its designated tensile strength. Moreover, this cracking stress is inversely proportional to about the fourth root of the size. For instance, a beam which has its

depth doubled in size will have its cracking strength decreased by a factor $0.5^{0.25} = 0.84$ [3].

According to the ACI, an estimation of the direct cracking strength, f_{cr}, can be obtained using the following empirical expression [3]:

$$f_{cr} = 0.33\lambda\sqrt{f'_c} \text{ in MPa} \tag{2.20}$$

where:

f'_c cylinder crushing strength

λ factor accounting for the density of the concrete

$\quad\lambda = 1.00$ for normal-weight concrete

$\quad\lambda = 0.85$ for sand-lightweight concrete

$\quad\lambda = 0.75$ for all-lightweight concrete

3

Basis Experiments

The specimens used as the subjects of this numerical investigation were taken from three past experiments on I-profile prestressed concrete beams. Those experiments are Hanson's (1964), Choulli's (2005) and Elzanaty's (1986). From all prestressed beams they studied, the author picked some of those beams that specifically experienced shear tension cracking during their tests. The description of the beams, the test procedure, and the result of each experiment were briefly described in this chapter.

3.1. Experiment by Hanson

John M. Hanson completed an experiment on prestressed concrete beams with web reinforcement as part of his graduation project as a Ph.D. student at Lehigh University in 1964. His research was based on the growing interest of studying the shear strength of concrete and the prestressed concrete beams around the early 1950s. The goal of his experiment was to assess the static ultimate shear strength of his prestressed members which were designed and fabricated as representative as possible to the actual precast prestressed bridge girders. The amount of web reinforcement and the length of the shear span were the two main variables of his investigation.

Test Specimens Description

Hanson conducted 38 tests on 23 doubly symmetric I-shaped cross-section prestressed concrete beams in his experiment. All twenty-three beams had 9 inches of flange width, 18 inches of total depth and a flange-to-web-width ratio of 3, which is shown in the beam cross-section picture in Figure 3.1. The prestressed concrete beams were referred to as the F series, ranging from F-X1 to F-22, and their deformation data was taken with a 5 inches and a 10 inches Whittemore Strain Gage.

The total span of the beam is divided into two segments: a test segment which was located between the supports and two reinforced anchorage segments which had a length of 1 feet at each end of the beams, as shown in Figure 3.1. In addition, all beams, except for F-17 and F-18, were also divided into three imaginary regions: Region A, B, and C, in which different vertical web reinforcement quantities were given. These regions, which will also be called the specimens in further descriptions, are labeled in a similar fashion as their beams, but with an additional letter at the end of the name which refers to the region's letter. For example, specimen A of the F-1 beam would be named F-1A, and in the same manner, its specimen B would be named F-1B.

Then, to apply the prestressing force, six high-tensile-strength strands with 7/16 inches diameter were used. These strands had a straight profile along the length of the beams which added 0.64 percent to the longitudinal-reinforcement ratio. Pretension was applied to each strand with a nominal initial force of 18.9 kips which gave the beams a total initial design prestressing force of 113.4 kips. The pretensioning caused the beams to have an initial tensile stress of 210 psi at the top fibers and an initial compressive stress of 2,150 psi at the bottom fibers.

SECTION PROPERTIES			
	Property	Value	Unit
A	Area	102.0	in^2
I	First Moment of Area	3854.0	in^4
Zt	Section Modulus (top)	428.2	in^3
Zb	Section Modulus (bot)	428.2	in^3
Qtf	Second Moment of Area (top flange)	262.5	in^3
Qcg	Second Moment of Area (mid)	286.5	in^3
Qbf	Second Moment of Area (bot flange)	262.5	in^3

Figure 3.1: Dimensions and Properties of F Series Test Beams (in Imperial Units)[6]

Test Procedure

Two types of testing procedure were used in the experiment: the concentrated load test and the uniform load test. The concentrated load test was applied on all prestressed concrete beams, except on F-17 and F-18. Each beam tested for the concentrated load test was typically tested in two stages. The end of the first stage was marked by any failure modes that a beam first experienced. The test was then stopped and the loads were lifted. After the first failure mode was recorded, the second stage of the test would be initiated on the remaining intact part of the beam and would end when that remaining part reached its ultimate limit state. In the test, the point loads were incrementally applied with the amount of approximately 5 percent of the expected failure load. After each load increment, the beam deflections would be recorded by level reading the targets proceeded to the nearest 0.01 inches.

On the other hand, the uniform load tests were given to beam F-17 and F-18 using the load arrangement shown in Figure 3.2. To simulate a uniform loading, two salvaged fire hoses filled with water were centered on the top flange of the beams. Then, four 8WF steel beams, with each had a length of a quarter of the total beam span, were used as loading beams to apply the distributed load from the hydraulic jacks. Lateral displacement between the ends of adjacent loading beams was prevented.

The concentrated load test itself had two different loading arrangements. The first arrangement, which shown in Figure 3.3, was applied on all beams designated for concentrated loading test, with an exception for F-20, F-21, and F-22 which used the loading arrangement in Figure 3.4. In the first loading arrangement, two point loads were applied to the beams which resulted in a constant moment region between the loading locations. In contrast, the second arrangement had a three-point loading system which divided one of the loading points in the first arrangement into two equal loads.

Figure 3.2: Testing Arrangement for Uniform Load Test (in Imperial Units) [6]

Figure 3.3: Testing Arrangement for All Concentrated Load Tests except for F-20, F-21 and F-22 (in Imperial Units) [6]

Figure 3.4: Testing Arrangement for Concentrated Load Tests on F-20, F-21 and
F-22 (in Imperial Units) [6]

Experiment Result

In conclusion, this experiment by Hanson showed that a prestressed concrete beam with an I-shaped cross section loaded with concentrated loads can have four different modes of shear failure: crushing of concrete in the web, shearing of the compression flange, fracture of the web reinforcement, and shear compression. The first three modes can occur because of the formation of inclined cracks that propagated entirely within a shear span, and the fourth mode can occur after an inclined crack penetrated the constant moment region that is adjacent to a shear span.

With the first concentrated loading arrangement, all beams experienced shear failures in their Region B at the end of the first stage of the test, except on F-9 which had a shear failure in Region A. Then, in the end the second stage, shear failures occurred in Region A of the tested beams, except on F-9 which have the shear failure in Region B.

Similarly, the second loading arrangement also caused shear failures in Region B of F-20, F-21 and F-22. Unfortunately, on the second stage of the test, none of the tested beams reached the expected shear strength. It was found that shear strength of these beams were reduced due to: the yielding of the strands during the first stage of test of these three beams, inclined cracks developing across existing flexural or shear tension cracks, and the loss of flexural bond strength. Thus, none of the test results from these beams were included in Hanson's dissertation.

In addition, it was concluded that the ultimate shear strength of a simply supported prestressed concrete beams with vertical web reinforcements under combined concentrated and distributed loadings can be predicted using the following equation [6]:

$$V_u = V_c + \frac{\beta d \, A_v \, f_y}{s} \tag{3.1}$$

where:

V_u ultimate shear strength at a section located a distance x from the support

V_c shear carried by the concrete, assumed equal to the shear causing significant inclined cracking

β_d effective horizontal projection of a significant inclined crack, assumed equal to the distance from the extreme fiber in compression (in composite beams from the top of the precast element) to the lowest level at which the stirrups are effective

A_v cross-sectional area of one stirrup

s spacing of stirrups

f_y yield point of the web reinforcement

Equation (3.1) can be used under the following assumptions:

- that the ultimate shear at any section which can be carried by the concrete is equal to the shear causing significant inclined cracking

- that the shear carried by the web reinforcement at the same section is equal to the force in the web reinforcement at the same section is equal to the force in the web reinforcement, stressed to the yield point, crossed by an idealized inclined crack.

3.2. Experiments used by Kroeze

In investigating the approach of Eurocode 2 1992-1-1:2004 for determining the capacity of a concrete structure in resisting shear tension crack, Kroeze (2018) made use of several past experiments on single-span I and T prestressed concrete beams tested by Elzanaty (1986) and Choulli (2005) as the basis of his numerical analyses. These experiments helped Kroeze to find the reason why the design of shear tension capacity using the Eurocode approach is often insufficient in practice and also to suggest a better model for designing the shear tension capacity. In modeling the specimens of these experiments on a finite element analysis software, Kroeze assumed that the beams behaved in a linear elastic manner until the first shear tension crack occurred.

3.2.1. Experiment by Choulli

In the hype of the development of Self-Compacting Concrete (SCC), Choulli did his experiment on prestressed concrete beams with an objective of finding specific mechanical properties of this new type of concrete mix. Specifically, he focused his research on gaining more understanding of the shear performance of prestressed concrete beams produced using the SCC. As a comparison, Choulli matched the SCC with a more commonly used concrete mix named the Conventional Vibrated Concrete (CVC) to find their differences in shear performance.

Test Specimens Description

Choulli conducted twelve experiments in his study by testing six prestressed beams at both of their ends. Each beam had the same monosymmetrical I-shaped cross-section, as shown in Figure 3.5, and had a length of 10 metres. Four beams were produced using the SCC and were named HAP1, HAP2, HAP1T, and HAP2T. The last two beams were created using the CVC and were named HCP1T and HCP2T. The beams were designed specifically to experience web-shear cracking under the combination of shear and bending. Specifically, HAP1 and HAP2 were designed without vertical reinforcements and had different prestressing reinforcement ratio.
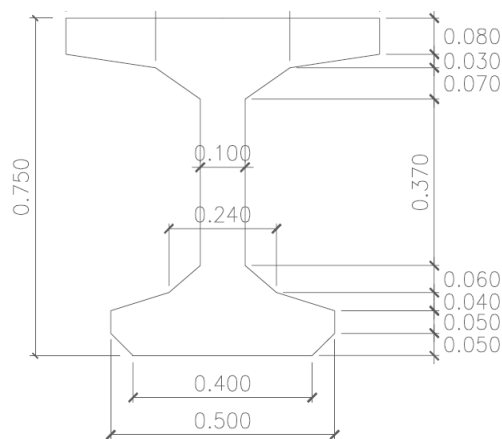
Figure 3.5: The Cross Section of All Choulli's Beams (in metre) [2]

Four essential variables were monitored in his experiment to allow him to observe their influences on the shear performance of the beam. Those variables are the type of concrete, the level of prestressing, the amount of longitudinal reinforcement in the web and the presence of vertical reinforcements. The vertical reinforcements were the Spanish standard B500S which have the yield strength (f_y) of 525 MPa and the ultimate strength (f_u) of 691 MPa. The longitudinal reinforcements, on the other hand, were the Spanish

standard B500SD with yield strength equal to 581 MPa and ultimate strength equal to 691 MPa.

For the prestressing strands, 0.5 inches in diameter Y1860S7 strands with 99 mm^2 sectional area were installed. Those prestressing strands had yielding strength $\left(f_{py}\right)$ and ultimate strength $\left(f_{pu}\right)$ of 1776 MPa and 1941.4 MPa, respectively. In HAP2, HAP2T, and HCP2T, ten strands were placed and in HAP1, HAP1T, and HCP1T, 16 strands were placed. Furthermore, the information about the concrete compressive and flexural strength is presented in Table 3.1 and the detail of the prestressing in each beam is presented in Table 3.2, where σ_{cp} is the average concrete stress due to prestressing.

Table 3.1: Compressive and Flexural Strength Properties of Choulli Beams [2]

Beam	Compressive Strength $\left(f_{cm}\right)$ (MPa)	Flexural Tensile Strength $\left(f_{ctm}\right)$ (MPa)	Modulus of Elasticity (E) (MPa)
HAP1	99.15	5.07	39,788
HAP2	96.34	5.01	42,409
HAP1T	91.23	4.91	39,855
HAP2T	95.97	5.00	39,569
HCP1T	81.00	4.68	33,675
HCP2T	90.24	4.89	39,788

Table 3.2: Choulli Beams Prestressing Details [2]

Beam	Amount of Strands	σ_{cp} Excluding Losses (MPa)	σ_{cp} Including Losses (MPa)
HAP1	16	11.37	9.56
HAP2	10	7.11	6.30
HAP1T	16	11.37	9.56
HAP2T	10	7.11	6.30
HCP1T	16	11.37	9.56
HCP2T	10	7.11	6.30

Test Procedure

As previously mentioned, every beam in this experiment was tested twice. Each beam had its left-end span treated as one specimen called the east-side specimen and the right-end span treated as another specimen called the west-side specimen. Each specimen has a span of 6.1 metres. The east side specimen had the same code name as its beam with a letter 'E' added to the end of the code name. Similarly, the west-side specimen also had the same code name, but with a letter 'W' instead added in the end.

Every test was set in a condition shown in Figure 3.6. All beams were simply supported with its fixed pin was put near the applied load and its sliding pin on the opposite side. The supports were spaced 0.6 metres from the end of a beam to ensure the anchorage of the pretensioned strands. Prior to the start of the data recording, 30 kN load was applied to a specimen to stabilize the test system.

The loads given to the beams were point loads. They were displacement controlled loads which were applied monotonically until the beams reached their failures. These loads were applied in a constant 2.1-metre distance from the support which was located near to the beam end. Particularly, when the west-side specimen of HAP1T and HCP1T had to be tested, their span had to be increased from 6.1 metres to 6.76 meters to guarantee an ultimate failure. An overview of shear-span-to-depth ratio of all specimens is given in Table 3.3.
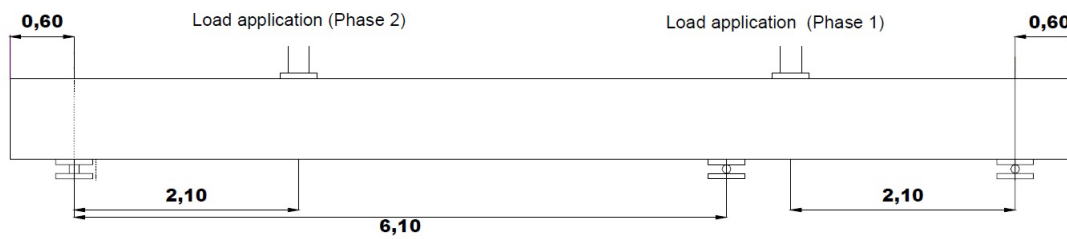
Figure 3.6: A Sketch of Choulli's Test Setup (in metre) [2]

Table 3.3: Shear-Span-to-Depth Ratio Overview [2]

Beam	Shear-Span-to-Depth Ratio (a/d)
HAP1	3.13
HAP2	3.00
HAP1T	3.13
HAP2T	3.00
HCP1T	3.13
HCP2T	3.00

Experiment Result

An overview of several test results from Choulli's experiment is presented in Table 3.4. The applied loads presented in that table are the loads that caused the specimens to exceed the linear elastic phase and experienced the first shear tension crack.

Table 3.4: Applied Loads and Shear Forces on Choulli Beams up to The First Shear Crack [2]

Beam	Applied Load (excluding 30kN)(kN)	Applied Load (including 30kN)(kN)	Shear Force (kN)
HAP1E	519	549	416
HAP1W	603	633	419
HAP2E	418	448	340
HAP2W	514	544	361
HAP1TE	508	538	409
HAP1TW*	635	665	438
HAP2TE	441	471	359
HAP2TW	529	559	368
HCP1TE	629	659	502
HCP1TW	579	609	421
HCP2TE	578	608	463
HCP2TW	580	610	404

*) a re-check calculation showed that the test configuration for this specimen had not been re-adapted

3.2.2. Experiment by Elzanaty

Elzanaty's research was part of numerous investigations in finding the correct properties of the high strength concrete. At that time, well-known building codes, such as the ACI code, provided engineers with only empirically derived criteria that were attained from extrapolating previously-tested normal-strength concrete. Therefore, further investigations on this new type of concrete were needed in order to allow engineers to design it better. Elzanaty focused his study on investigating the effect of using high-strength concrete on the shear strength of reinforced and prestressed concrete beams and also compared his test results with the established design code provisions at that time.

Test Specimens Description

Fifty-three beams in total produced using high-strength concrete were experimented by Elzanaty. These beams were divided into two groups: nineteen rectangular reinforced concrete beams were in the first group and thirty-four prestressed concrete beams were in the second group. The variables in this experiment were the concrete strength, the longitudinal reinforcement ratio, the shear-span-to-depth ratio, and the amount of shear reinforcement.

The group of prestressed concrete beams was then divided again into another two groups based on their cross-section, as shown in Figure 3.7. They are the CW series and the CI series which consisted of 17 beams each. Particularly, CW/CI 10 until CW/CI 17 had vertical reinforcements installed while the others were not.

(a) CI series   (b) CW series
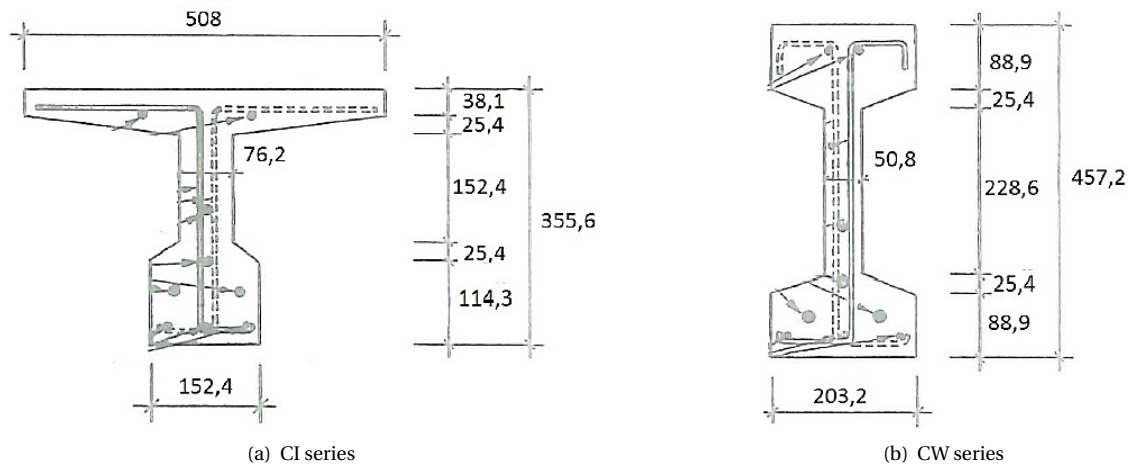
Figure 3.7: Cross Section of Elzanaty's Prestressed Concrete Beams (in mm) [4]

Because only CW series beams that were used in this study, from here on the descriptions are focused solely on this beam series. The detail of CW series beams compressive strength is provided in Table 3.5 and their prestressing detail in Table 3.6. For the prestressing strands, low relaxation seven-wire grade 270 strands were used. Each CW beam had four this type of strands installed in them. The location of these strands inside a CW beam is shown in Figure 3.8.
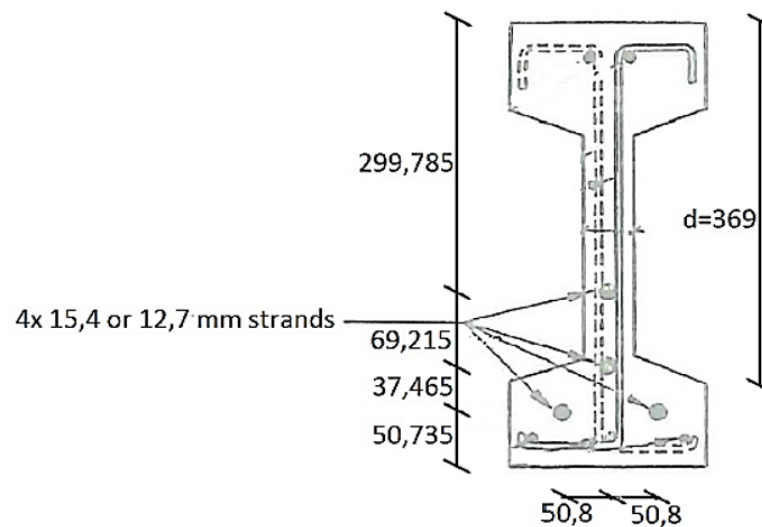
Figure 3.8: Orientation of CW Series Strands [4]

Table 3.5: Compressive Strength of CW Series Beams [4] [5]

Beam	Compressive Strength (f_{cm}) (MPa)	Flexural Tensile Strength (f_{ctm}) (MPa)
CW1	76.55	4.58
CW2	76.55	4.58
CW3	76.55	4.58
CW4	78.62	4.63
CW5	77.93	4.61
CW6	77.93	4.61
CW7	77.59	4.60
CW8	41.38	3.35
CW9	61.03	4.16
CW10	73.08	4.49
CW11	55.86	4.00
CW12	39.99	3.27
CW13	72.41	4.47
CW14	73.79	4.51
CW15	70.34	4.42
CW16	73.10	4.49
CW17	69.66	4.40

Table 3.6: Prestressing Detail of CW Series Beams [4] [5]

Beam	Strand Diameter (mm)	Strands Cross-Sectional Area (mm^2)	Effective σ_{cp} (MPa)
CW1	15.4	568	11.20
CW2	15.4	568	11.13
CW3	15.4	568	11.01
CW4	15.4	568	11.60
CW5	15.4	568	11.18
CW6	15.4	568	8.40
CW7	12.7	395	8.19
CW8	15.4	568	8.33
CW9	15.4	568	8.25
CW10	15.4	568	8.40
CW11	15.4	568	8.20
CW12	15.4	568	8.20
CW13	15.4	568	11.50
CW14	15.4	568	11.60
CW15	12.7	395	8.20
CW16	15.4	568	11.60
CW17	15.4	568	11.60

Test Procedure

For the test, all CW series beams were given a setup as shown in Figure 3.9. The setup was depended on the beams dimensions which were determined according to their shear-span-to-depth ratio (a/d). The shear spans of these beams had several values, as shown in Table 3.7, while the depth of the beams was constant at 369 mm. Furthermore, these beams were all simply supported with a fixed pin bearing put near the applied load and a sliding pin bearing on the other side. Both supports were placed 381 mm from the beam ends.

Moreover, the loads which were applied to the beams were point loads. These point loads were applied incrementally until the beams reached their ultimate limit state. As for specimens that had no stirrups, the

point loads were given in the increments of 22.2 kN until failure occurred for CW beams and until flexural cracks appeared, alternatively, for CI beams. On the other hand, the same load increment was applied for specimens with stirrups, but only until failure was almost reached and then smaller load increment was used until the ultimate limit state was reached.
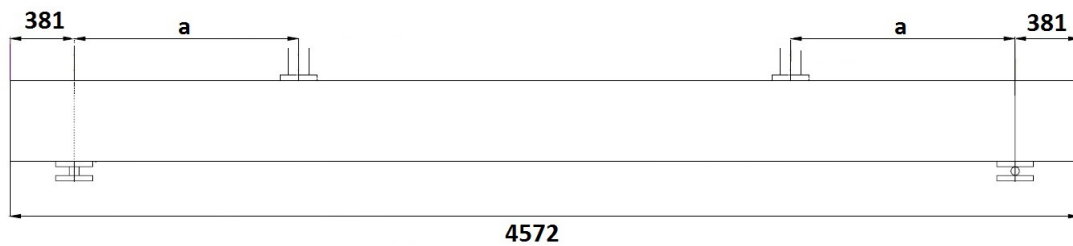
Figure 3.9: A Sketch of CW Series Beams Test Setup [4]

Table 3.7: Shear-Span-to-Depth Ratio for CW Beams [5]

Beam	Shear-Span-to-Depth Ratio (a/d)	a (mm)
CW1	2.90	1070
CW2	3.75	1384
CW3	5.00	1845
CW4	3.75	1384
CW5	3.75	1384
CW6	3.75	1384
CW7	3.75	1384
CW8	3.75	1384
CW9	3.75	1384
CW10	3.80	1402
CW11	3.80	1402
CW12	3.80	1402
CW13	3.80	1402
CW14	3.80	1402
CW15	3.80	1402
CW16	3.80	1402
CW17	3.80	1402

Experiment Result

Partial results of Elzanaty's experiment for CW series beams are presented in Table 3.8. The shown results were limited only to loads that caused the CW specimens to experience their first shear tension crack. At the applied load level, shear tension crack quickly appeared throughout the depth of the web from the top web-flange junction to another web-flange junction at the bottom. It propagated in the region of a shear span from a support location to the load point with an angle ranged from 15 to 30 degrees. As for beams without stirrups, a shear tension crack represented the ultimate shear strength of the beams and, additionally, it is only CW6 beam that had a single flexural crack when the shear crack appeared.

Table 3.8: Applied Load and Shear Force on CW Series Beams up to The First Shear Crack [4]

Beam	Applied Load (kN)	Shear Force (kN)
CW1	138.33	138.33
CW2	124.55	124.55
CW3	117.43	117.43
CW4	127.22	127.22
CW5	124.11	124.11
CW6	112.10	112.10
CW7	105.87	105.87
CW8	89.85	89.85
CW9	100.97	100.97
CW10	108.54	108.54
CW11	95.64	95.64
CW12	85.41	85.41
CW13	122.77	122.77
CW14	123.66	123.66
CW15	100.53	100.53
CW16	122.33	122.33
CW17	123.22	123.22

4

Proposed Approaches for Investigating The Size Effect

For this study, the author proposes two new approaches for studying the size effect in shear tension cracking, namely the σ_1 area approach and the ratio-of-distances approach. These approaches are essential for this numerical investigation since there were only experimental samples available to the author and there was no established approach yet for studying the size effect in shear tension cracking when the author started this study. The aim of these approaches is to help the author to find an explanation that can describe the influence of structural size to the deviation of the uniaxial tensile strength in an I-profile prestressed concrete beam.

4.1. σ_1 Area Approach

The σ_1 area approach is a technique for detecting a structural size dependency of the uniaxial tensile strength by finding the relation between the size of σ_1 areas with the maximum principal tensile stress (σ_{1max}) of a number of shear cracks that is normalized with the concrete mean uniaxial tensile strength (f_{ctm}). The σ_1 area is a rectangle that represents a group of σ_1 values that have a higher likelihood in achieving the deviated value of f_{ctm} and initiate shear tension cracking on the web of a prestressed concrete beam. The length of this rectangle is the distance between two intersection points made by a plot of the σ_1 along a shear tension crack and a constant line of the reduced value of maximum principal tensile stress $(\sigma_{1max,red.})$. That length is then multiplied with the beam's web thickness to form a rectangle. The $\sigma_{1max,red.}$ value is set at 90% of σ_{1max} under an assumption that it is more likely for maximum principal tensile stress above $\sigma_{1max,red.}$ value to trigger shear tension cracking. An illustration of the σ_1 area is shown in Figure 4.1.

Subsequently, every σ_1 rectangle is compared with another rectangle created from other shear cracks. The comparison shown in a graph of normalized maximum principal tensile stress (σ_{1max}/f_{ctm}) of each crack vs. the σ_1 rectangles area allows the size effect on the f_{ctm} values to be observed. f_{ctm} is size dependent when there is a significant decremental differences of σ_{1max}/f_{ctm} values along the axis of the areas, and conversely, f_{ctm} is size independent when σ_{1max}/f_{ctm} is relatively constant along that same axis.

The idea for creating this approach was based on the deviation of material properties in a structure. In reality, every element in a structural body has its strength diverged from its designated value after the structure is constructed. Because of this, it is possible that a shear crack can propagate through each element that fails at a lower uniaxial tensile strength level due to the stresses generated by the acting loads. This means that the longer a potential crack length is, the more elements and the more material strength randomness that the shear crack encounters. Based on this fact, an area made of multiplication between a potential crack length and a web thickness can be used to study the size effect.
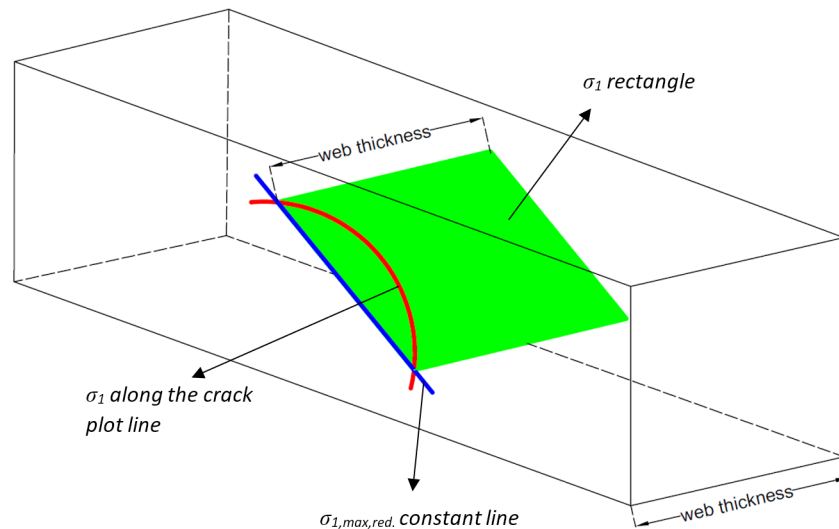
Figure 4.1: An Illustration of σ_1 Rectangle

4.2. Ratio-of-Distances Approach

In ratio-of-distances approach, the size effect in shear tension cracking is investigated by observing the locations of σ_{1max} where a shear tension crack initiated in the web of each studied prestressed concrete beam. This approach was created based on the assumption that a shear tension crack is more likely to originate from near the beam neutral axis instead of near the web-flange junction due to the change of thickness at that interface. Therefore, it is also more probable for σ_{1max} to be located near a beam neutral axis.

The result of the investigation is given in the form of a graph that relates the volume of the web part of a prestressed concrete beam and the ratio of distances $\left(\ell_{\sigma_{1max}}/\ell_{c.o.g.}\right)$. The ratios of distances, which are presented at the vertical axis of the graph, show a quantitative relation between the vertical distance from σ_{1max} location to the web-flange junction $\left(\ell_{\sigma_{1max}}\right)$ and the vertical distance from the same web-flange junction to the beam's neutral axis $\left(\ell_{c.o.g.}\right)$, as presented in Figure 4.2. The ratio gives a normalized value that represent the location of σ_{1max} between the neutral axis and the web-flange junction. In the horizontal axis of the graph, the web-part volumes represent the structural size differences between each investigated beam and it is calculated using the web width, the web length and the shear span of each studied beam. The web-flange junction used for this purpose is the junction at the observed area that has the closest distance to the extreme tensile fiber of a beam.

As a result, it is expected that the size effect can cause a prestressed concrete beam to have shear tension cracking that originates closer to the web-flange junction. The reason is that the uniaxial tensile strength in a larger beam should have a larger strength deviation, and therefore, there is a possibility that σ_{1max} can encounter a lower uniaxial tensile strength near the web-flange junction and a shear tension crack occurs from that location.
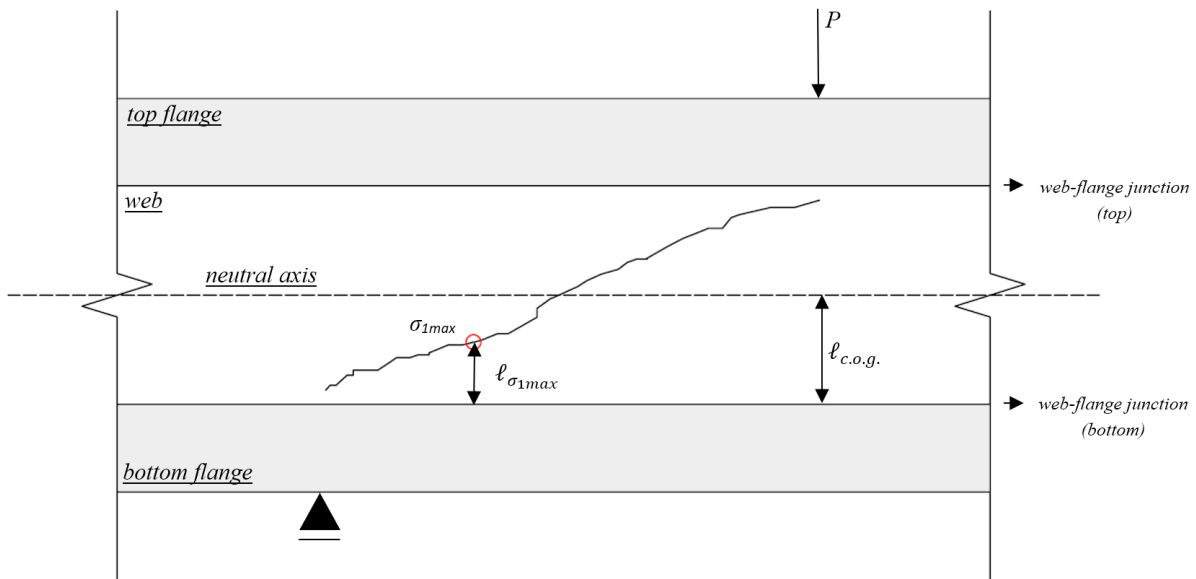
Figure 4.2: An Illustration of $\ell_{\sigma_{1max}}$ and $\ell_{c.o.g.}$.

Numerical Investigation into Size Effect in Shear Tension Cracking

5.1. LEFEA on Hanson's Beams

As part of the investigation, several test samples from a past experiment mentioned in Chapter 3 were re-assessed using finite element analysis (FEA). Those samples are the prestressed concrete beams tested by Hanson (1964) which experienced shear tension cracking at their web of Region A and B, which will also be called the specimen A and B in further descriptions. The shear tension cracks were the result of the first stage of a 4-point bending test, especially, the test which used the first concentrated loading arrangement, as mentioned in subchapter 3.1. After being reassessed, only some of the specimens of the test samples were going to be used for further analyses. The selected specimens are presented in Table 5.1.

The test samples were remodeled on DIANA FEA 10.1 and reanalyzed using linear elastic finite element analysis (LEFEA). The analysis aimed to obtain nearly realistic principal tensile stress distribution at the region where a shear tension crack formed. The choice for using linear elastic analysis was based on the information mentioned by Hanson in his dissertation [6] that the shear tension cracks were the first cracks the specimens experienced, and therefore, the specimens should be analyzed in the service limit state (SLS) which lays on the linear elastic region as stated in the Eurocode 2.

Nearly realistic principal tensile stresses were essential data for this study because the information about the principal stress distribution provided by Hanson in his dissertation [6], as shown in Figure 5.1 as an example, was deemed to be unreliable for studying the size effect. It is unreliable because Hanson calculated these principal stress values using analytical calculations which were based on the Bernoulli theory. It is safe to assume that Hanson did the analytical analyses to obtain those stresses instead of numerical analysis because of the limited computer capacity at his era to do a finite element analysis. Consequently, the principal stresses values printed in Figure 5.1 did not represent the stress distribution at the beam's disturbed regions correctly.

5.1.1. Properties of The Finite Element Models

As part for the inputs to the finite element models, the properties of the test samples, such as the cross-section, dimension, and material characters were inserted into the finite element software. These properties helped the finite element models, which were built with several simplifications, to mimic the actual behavior of the beams under the 4-point bending test and to generate the principal tensile stresses that are somewhere close to the reality.

The cross-section, as one of the properties, were inputted into DIANA FEA using a function, as shown in Figure 5.2. This function then drew half of the cross-section which then used as the element geometry of the beam model after it was multiplied by 2. Since all Hanson's beams had same I-shaped profile as shown in the
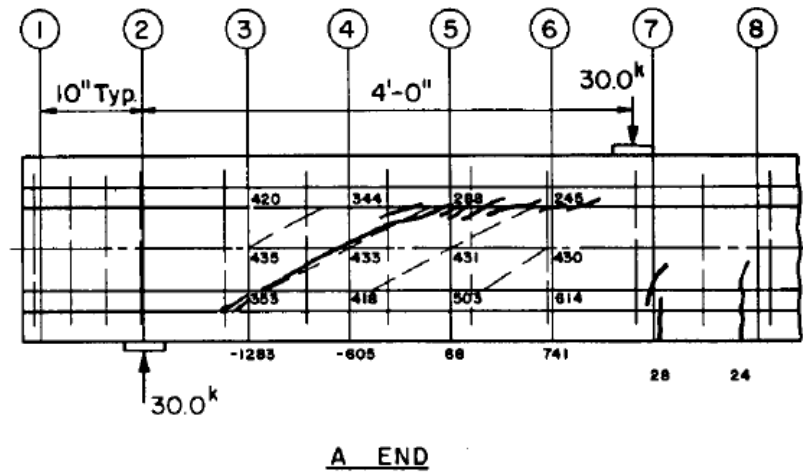
Figure 5.1: Hanson's F-X1A Specimen with Crack

cross-section picture in Figure 3.1, the same element geometry was applied to all models of the test samples.
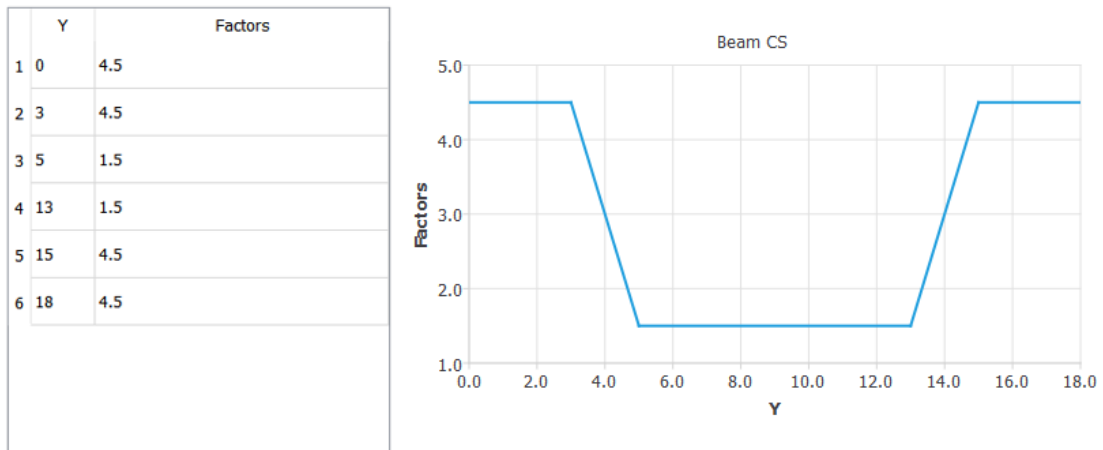
Figure 5.2: Cross-Section Function in DIANA FEA

Next, the dimension and material properties were also typed into the software as parts of the properties of the finite element models. In his experiment, Hanson gave each of his specimen unique dimensional and material properties in order to allow him to study the ultimate shear strength of the prestressed beams. Hence, every model built for the numerical analyses of this study had a particular test span and Young's modulus, as shown in Table 5.1. Nevertheless, since all prestressed beams were made of concrete, all specimens had the same density and Poisson's ratio of 2,500 kg/m^3 and 0.2, respectively.

Besides the aforementioned properties, the other beam character which was used for further crack analyses but was not inputted into the models was the strength property. That essential strength property is the mean uniaxial tensile strength $\left(f_{ctm}\right)$ which were used as a comparison to the principal tensile strength (σ_1). Since there was only information about the compressive strengths of the beams $\left(f_c'\right)$ in the dissertation[6], f_{ctm} values had to be derived analytically using several formulas from Eurocode 2. For that purpose, Equation 2.19 can be used to determine the characteristic cylinder strength or f_{ck} $\left(f_c' = f_{cm}\right)$. The calculation using that equation showed that all selected specimens had characteristic strengths below C50/60 which means that equation 2.17 can be used to define the f_{ctm} values from the provided f_c' values. All f_c' and f_{ctm} values of the selected specimens are presented in Table 5.1.

Table 5.1: Properties of The Selected Specimens of Hanson's

Specimen	Length (mm)			$f_c' = f_{cm}$ (N/mm²)	f_{ctm} (N/mm²)	E_c (N/mm²)
	Specimen Length	Test Span	Total Span			
F-X1A	1219	3708	4318	45.9	3.62	27579
F-X1B	1219	3708	4318	45.9	3.62	27579
F-1A	762	2794	3404	47.0	3.68	29647
F-1B	762	2794	3404	47.0	3.68	29647
F-2A	1016	3302	3912	45.2	3.58	26200
F-2B	1016	3302	3912	45.2	3.58	26200
F-3A	1016	3556	4166	47.2	3.69	22753
F-3B	1016	3556	4166	47.2	3.69	22753
F-4B	1270	3810	4420	43.7	3.49	28958
F-5A	1270	4064	4674	44.2	3.52	26200
F-5B	1270	4064	4674	44.2	3.52	26200
F-19A	1270	5080	5690	51.1	3.91	27579

5.1.2. Finite Element Modeling

The finite element models were generated based on the mechanical model of Hanson's prestressed beams. More specifically, the mechanical model is a simply-supported prestressed concrete beam which had a 4-point bending test as its physical problem. It has a great resemblance to its physical model with several simplifications as presented in Figure 5.3(b). Those simplifications came in the form of point loads and point supports as a form of idealization to the actual condition which helped to simplify the numerical analysis.

(a) Physical Model
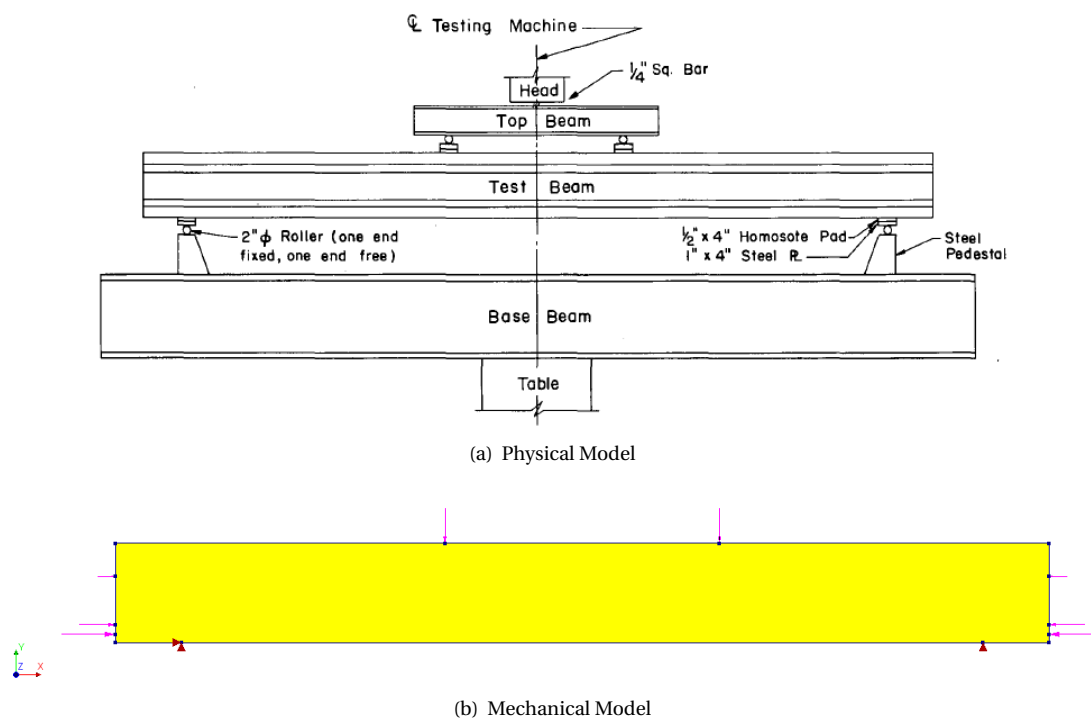
(b) Mechanical Model

Figure 5.3: The Physical Model and The Mechanical Model of Hanson's Beams

The point loads in the mechanical model helped to idealize the external forces that worked on the pre-stressed beams. Those external forces can be categorized as the cracking loads and the prestressing loads. The cracking loads are concentrated vertical loads which were applied with the configuration of the first loading arrangement, as shown in Figure 3.3. In the finite element models, the point loads were inputted with a magnitude that induced the formation of shear tension crack on the specimens. The location of these symmetrical point loads on the models depended on the length of the test span, which also simultaneously defined the length of specimen A, B, and C.

On the other hand, the prestressing loads are symmetrical horizontal loads which were generated by six pretensioned-high-tensile-strength strands which were installed in 3 different levels inside the experimented beams, as shown in the cross-section picture in Figure 3.1. The strands were not modeled as bonded tendons in the finite element model because the specimens were analyzed in a linear elastic region, and therefore, modeling the reinforcement and the prestressing tendons became unnecessary. The values of the cracking load per load point and the total prestressing force on each selected specimens are available in Table 5.2.

Table 5.2: The Cracking Loads and The Prestressing Loads on The Selected Specimens

Specimen	Cracking Load per Load Point (kN)	Total Prestressing Force (kN)
F-X1A	133	408
F-X1B	126	408
F-1A	146	411
F-1B	150	411
F-2A	151	384
F-2B	133	384
F-3A	138	390
F-3B	125	390
F-4B	142	421
F-5A	124	387
F-5B	124	387
F-19A	133	399

In a similar manner, the supports were also idealized as point supports in the finite element models. The point support acted as the boundary conditions for the models and located at 1 foot or 304.8 mm from the beam ends. Their distance from each other varies following the length of their beam's test span.

Besides the simplification on the loads and the supports, the beam itself was also simplified into 2D models in the numerical analysis. The 2D models were realized using quadratic quadrilateral plane stress elements which were chosen by the author to model the discretization of the prestressed beams. The quadratic elements, which has a code name of CQ16M, was picked to help the models obtaining nearly realistic stress distributions and displacement results. Specifically, CQ16M has 8 nodes in total, with 4 corner nodes and 4 middle nodes. At each node, the element has two degrees of freedom (DOF) which have directions to the x and y-axis of its coordinate system. By default, CQ16M has 2 x 2 integration points and uses the Gauss integration scheme in DIANA FEA 10.1, as shown in Table 5.3.

In addition, this quadratic element also includes shear deformation in analyzing the deformation of the element. The inclusion of shear deformation means that the finite element models automatically incorporated deflections due to shear into the total deflection of the beam.

Table 5.3: The Detail of CQ16M

FE type	DOF	Interpolation Scheme	Integration Scheme	Shape / Topological Dimension	Stress Components	Include Shear Deformation
CQ16M (8-noded quadratic plane stress elements)	16 (u_x and u_y per node)	Quadratic	2x2 Gauss Intergration	2D / 2D	SXX, SYY, SXY	Yes

As for the mesh generation, the element size was selected to be 0.25 inches or 6.35 mm. This element size can be considered to be a very fine size, as can be seen in Figure 5.4. The determination of this element size was based on practicality issue for later rearrangement of DIANA FEA's output data using a Python script which is presented in Appendix B. It was governed by the location of the prestressing loads due to their center-to-center distances which are the multiples of 0.25 inches. As a verification to the accuracy of the FEA result, a plot of element size vs. maximum midspan deflection is presented in Figure 5.5. It shows that the FEA results have reached convergence by showing negligible differences (0.01-0.02 mm) between each maximum midspan deflection result which were produced by the finite element models at element size of 50.8 mm, 25.4 mm, 12.7 mm, and 6.35 mm. Unfortunately, the plot line does not show a normal convergence curve which most probably caused by local deformation at the location of the point supports due to their idealization.
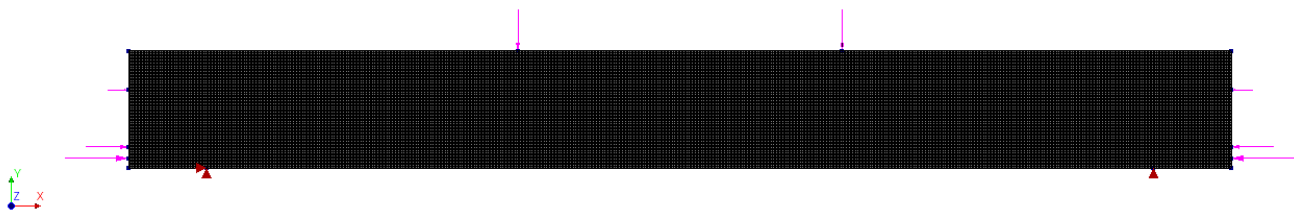
Figure 5.4: Meshed Finite Element Model of F-X1A
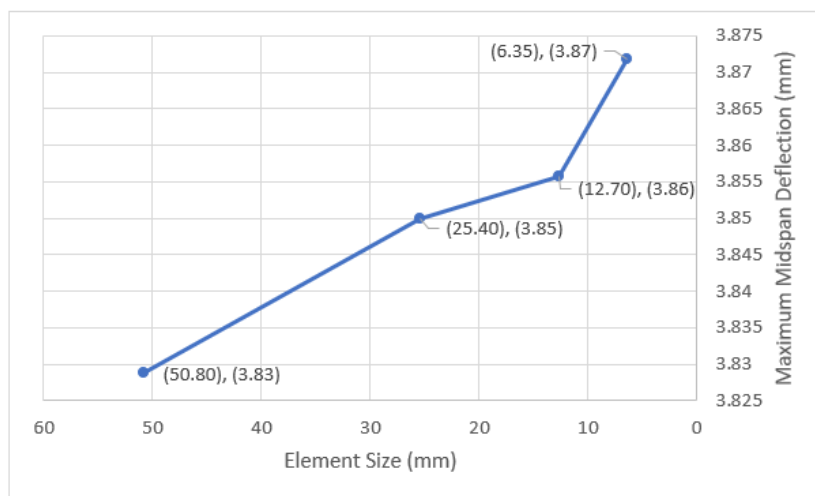
Figure 5.5: Element Size vs. Maximum Midspan Deflection of F-X1A

After the modeling of the test samples were complete and the meshes have been generated, LEFEA was run to obtain the results. The linear elastic analysis provided several output data including the principal tensile stresses (σ_1) which were used for the study of size effect. All output data were collected from the nodes and nodal averaging function was not activated.

Since there were only several specimens from the tested samples that were going to be included in further size effect study, the output data were grouped based on their region. From each group, only the data that originated from the elements inside a shear span of a region were used. An example of selected elements for output data collection is shown in Figure 5.6 for F-X1A specimen model.
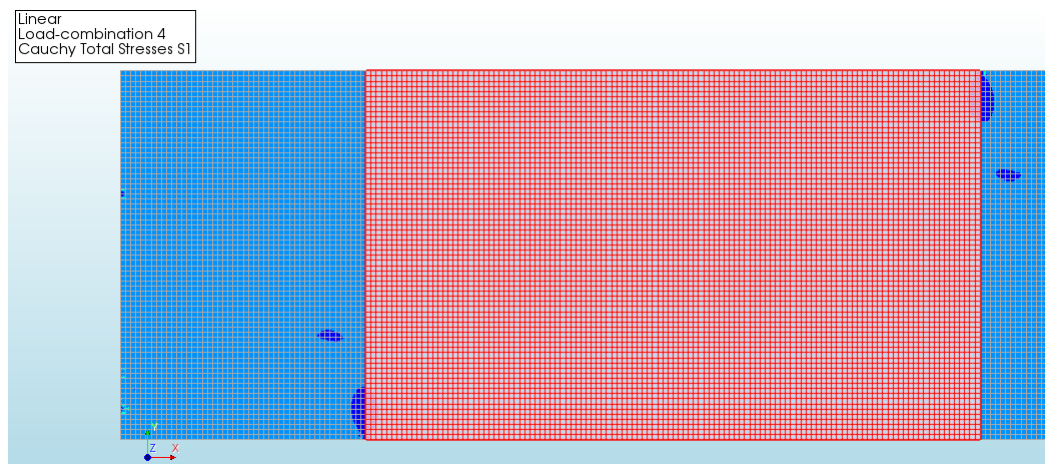
Figure 5.6: Selected Elements (in Red) in The Shear Span of F-X1A Specimen
Model

5.1.3. Rearrangement of DIANA FEA Output Data

Since the principal tensile stress data outputted by DIANA FEA came in bulk and was sorted based on the order of the element number (element-id), it was necessary to rearrange this data to allow the author to study the size effect more conveniently. The data bulk came from every node which contained four σ_1 values originating from one of the integration points in the elements connected to the node. The data rearrangement was done with the help of a Python script, which can be found in Appendix B, and it went through the several steps: data reorganization based on its nodal coordinates, removal of redundant data, and manual nodal averaging.

The reorganization of σ_1 data according to its nodal coordinates set these quantities into their actual position in a shear span of a specimen model, as presented in Figure 5.7(b). In this step, the author chose to remove the σ_1 data from the middle nodes of each element to reduce the amount of data to analyze. The σ_1 data from the corner nodes was deemed sufficient to represent the stress distribution of the specimens due to the fine size of the elements. By having this new arrangement, the data formed a mirror image for a specimen's finite element model at which the location of the shear tension crack at the web of the specimen can be re-imagined on the mirror image, and thus, the σ_1 values along the crack can be obtained and studied. The process of crack re-imagination at this data set is explained in subchapter 5.3.

Furthermore, after the σ_1 data was reassigned to its nodal coordinates, it went through an elimination process in the Python script to remove some redundant principal tensile stress data. The elimination was done by removing one row of elements (the outer row) which was located precisely outside the web area at each web-flange junction of the I beams. The removal was a necessary step in order to disregard the outliers in the σ_1 data which existed due to an abrupt change of geometry at the web and flange interfaces. If compared to the σ_1 data originated from an element row adjacent to the eliminated row (the inner row), these outliers have a significant difference in value which can be up to 30%. By deleting these rows of elements, each node from the inner rows that previously shared with the elements from the outer rows will then collect

(a) DIANA FEA σ_1 Output Data of F-X1A's

	Beam Length (in.)												
	12 (**)	12.25	12.5	12.75	13	13.25	13.5	13.75	14	14.25	14.5	14.75	15
18 (*)	180.36	173.63	166.34	158.49	150.08	141.11	131.58	121.50	110.87	99.71	88.03	75.82	63.12
17.75	137.48	130.90	123.81	116.23	108.14	99.56	90.51	81.00	71.06	60.75	50.16	39.46	29.01
17.5	96.70	90.55	84.02	77.13	69.93	62.48	54.88	47.28	39.87	32.96	26.85	21.78	17.83
17.25	59.69	54.77	49.80	44.87	40.11	35.64	31.59	28.01	24.95	22.39	20.26	18.50	17.04
17	31.46	29.29	27.35	25.65	24.16	22.88	21.78	20.83	20.02	19.31	18.68	18.13	17.64
16.75	16.76	16.85	16.97	17.11	17.26	17.41	17.56	17.71	17.85	17.97	18.09	18.18	18.26
16.5	9.91	10.82	11.70	12.56	13.39	14.18	14.93	15.65	16.33	16.97	17.56	18.11	18.62
16.25	5.57	6.79	8.02	9.22	10.41	11.58	12.71	13.81	14.86	15.88	16.84	17.75	18.62
16	1.96	3.36	4.78	6.21	7.65	9.08	10.49	11.88	13.24	14.56	15.83	17.06	18.24
15.75	-1.48	0.03	1.60	3.20	4.83	6.47	8.12	9.75	11.37	12.95	14.51	16.02	17.48
15.5	-4.97	-3.37	-1.68	0.06	1.85	3.68	5.52	7.37	9.22	11.05	12.86	14.63	16.36
15.25	-8.62	-6.93	-5.14	-3.27	-1.33	0.66	2.68	4.73	6.79	8.84	10.88	12.90	14.88
15	-12.43	-10.67	-8.79	-6.81	-4.74	-2.61	-0.42	1.81	4.06	6.32	8.58	10.83	13.04

note: (*) : beam top
(**) : left support location

(b) Partial Sample of Rearranged F-X1A's σ_1 Output Data

Figure 5.7: Rearrangement of DIANA FEA Output Data

only two σ_1 data that comes from the integration points of the elements in the inner row.

The issue of redundant σ_1 values at the web-flange interface has also been brought up by Kroeze (2018) in his report. In the same manner, he also removed the outer row of elements in the web-flange junction of a HAP1E beam cross-section and other I beam models in order to obtain more realistic σ_1 results from his finite element models. An example of a deleted outer row from a HAP1E model, which is colored in red, is presented in Figure 5.8.

Additionally, to make sure that the Python script has done the elimination process correctly, the author created a manual check using Ms. Excel by coloring the excel sheets provided by the Python script that contains information about the number of data collected by each node. Nodes that had collected only two σ_1 data will be colored red, the ones that had collected only one σ_1 data will be colored green and the ones with four σ_1 data will be colored yellow. In Figure 5.9, a check on F-X1A specimen FEA result showed that the nodes that were previously connected with the outer row had a red color which means that they only carried two data with them.
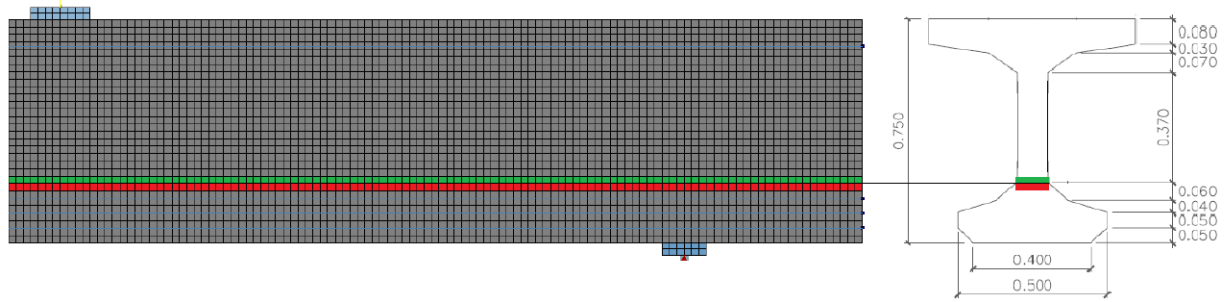
Figure 5.8: A Row of Elements at Web-Flange Interface which was Removed from HAP1E Model[8]
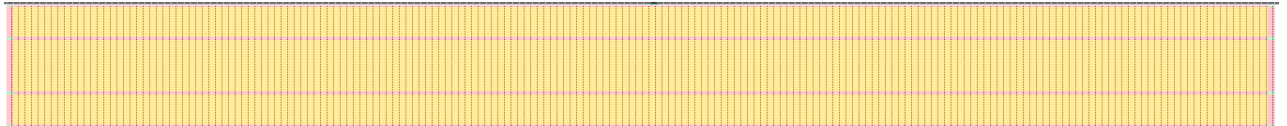
Figure 5.9: Elements Removal Check on F-X1A Specimen Model

Besides restructuring and eliminating data, the Python script also simultaneously averaged the principal stress data possessed by each node. The averaging has to be done manually since the nodal averaging function was not used during the linear analysis. As a result, every node had only one σ_1 value that used for studying the size effect.

5.2. FEA Result Verification with Analytical Checks

Since DIANA FEA is just a tool to do numerical analyses, it is necessary to check if the inputs that had been inserted into the software had generated the correct results. This type of check is often known as the sanity check. The sanity check for this study was done by comparing the numerical results with the results from analytical calculations. The analytical calculations produced the exact values instead of the estimated values generated by the finite element software for the same physical problem.

The sanity check was conducted on the principal tensile stress distributions in the non-disturbed region, or also known as the Bernoulli region, of the specimens. The check was not done in the disturbed region since the stress distribution in that area is irregular due to the nonlinear distribution of the normal stress and shear stress components. The author chose the F-X1A specimen to be the subject of this verification and it became the reference model for the other specimens.

The analytical results of the principal tensile stress distributions were obtained through a series of calculations. Before the principal tensile stress distributions could be obtained using Equation 2.12, the normal stress and shear stress components had to be defined first using Equation 2.2, 2.3, and 2.4 based on the physical problem of F-X1 beam, as shown in Figure 5.10. The values of the normal stress and the shear stress components along the shear span of F-X1A were the results of the point loads and the prestressing loads acting on the F-X1.
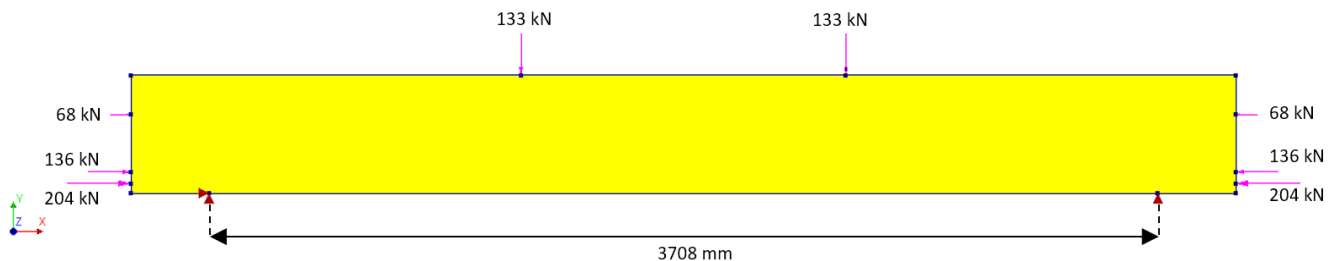
Figure 5.10: F-X1 Physical Problem

As previously mentioned in subchapter 2.2, due to the relatively small contribution of the normal stress components to the y-axis direction in a beam, σ_1 values can be found using Equation 2.13 instead of Equation 2.12. The σ_1 values resulted by Equation 2.13 is presented in Table 5.4. As a comparison, the σ_1 values generated from the numerical analysis of F-X1A in DIANA FEA is presented in Table 5.5.

Table 5.4: F-X1A's σ_1 Analytical Values Along Its Shear Span

Height Coordinate from c.o.g. (mm)		Length Coordinate (mm)					
		304.8	558.8	812.8	1066.8	1320.8	1524.0
-228.60		1.44	0.00	0.00	0.00	0.00	0.00
-101.60		3.64	2.94	2.41	2.02	1.72	0.00
-88.90		3.59	2.99	2.52	2.16	1.87	0.00
-76.20		3.53	3.02	2.62	2.29	2.02	0.00
-63.50		3.46	3.05	2.71	2.42	2.17	0.00
-50.80		3.39	3.07	2.79	2.54	2.33	0.00
-38.10		3.31	3.07	2.85	2.66	2.49	0.00
-25.40		3.22	3.06	2.91	2.77	2.64	0.00
-12.70		3.12	3.04	2.96	2.88	2.80	0.00
0.00	Neutral Axis	3.02	3.01	2.99	2.98	2.97	0.00
12.70		2.91	2.97	3.02	3.07	3.13	0.00
25.40		2.80	2.91	3.03	3.16	3.30	0.00
38.10		2.68	2.85	3.03	3.24	3.47	0.00
50.80		2.56	2.77	3.02	3.31	3.64	0.00
63.50		2.43	2.69	3.00	3.37	3.81	0.00
76.20		2.29	2.60	2.97	3.43	3.99	0.00
88.90		2.16	2.49	2.92	3.47	4.18	0.03
101.60		2.02	2.38	2.86	3.51	4.37	0.87
228.60		0.00	0.00	0.00	0.92	5.80	9.70

σ_1 ana.

Table 5.5: F-X1A's σ_1 Numerical Values Along Its Shear Span

Height Coordinate from c.o.g. (mm)		Length Coordinate (mm)					
		304.8	558.8	812.8	1066.8	1320.8	1524.0
-228.60		1.24	0.00	0.00	0.00	0.00	-14.71
-101.60		-0.27	2.70	2.53	2.02	1.16	-5.62
-88.90		-0.43	2.71	2.64	2.16	1.27	-4.91
-76.20		-0.59	2.71	2.73	2.30	1.39	-4.28
-63.50		-0.75	2.70	2.82	2.44	1.51	-3.72
-50.80		-0.92	2.69	2.89	2.57	1.65	-3.21
-38.10		-1.10	2.67	2.95	2.70	1.78	-2.73
-25.40		-1.28	2.65	3.00	2.82	1.93	-2.29
-12.70		-1.48	2.62	3.04	2.93	2.09	-1.86
0.00	Neutral Axis	-1.68	2.58	3.06	3.04	2.25	-1.45
12.70		-1.90	2.54	3.08	3.14	2.42	-1.04
25.40		-2.14	2.50	3.08	3.24	2.60	-0.65
38.10		-2.40	2.44	3.07	3.32	2.78	-0.25
50.80		-2.69	2.38	3.05	3.40	2.98	0.15
63.50		-3.00	2.31	3.02	3.48	3.18	0.56
76.20		-3.36	2.23	2.98	3.54	3.39	0.97
88.90		-3.74	2.15	2.93	3.60	3.62	1.40
101.60		-4.16	2.05	2.86	3.64	3.86	1.84
228.60		-10.00	0.00	0.00	1.01	6.40	9.76

σ_1 num.

The comparison between the analytical and the numerical values of σ_1 along F-X1A's shear span is presented in the form of percentages which indicated the level of similarity between the two. The result of the

comparison is shown in Table 5.6. Since the sanity check was designated only for the σ_1 values in the Bernoulli region of the specimen, differentiation on the percentages based on their location in the regions had to be done. The percentages located on the disturbed region was colored in blue that ended at a beam height distance (18 inches or 457.2 mm) from the location of the left point support and the left point load of F-X1 beam finite element model, and conversely, the percentages located on the Bernoulli region was colored in red.

The result of the comparison in the red columns of Table 5.6 showed a high degree of similarity between the numerical values and the analytical values of σ_1 with the percentages ranging from 91.11% to 100.06%. This means that the finite element model had passed the sanity check and given the correct values as expected through the analytical calculations.

The 0% values in the red columns didn't mean that the comparison showed a dissimilarity between both. In fact, their analytical and numerical values are very similar, but they are zeros, as shown in Table 5.4 and Table 5.5. Thus, because the comparisons were made by dividing the analytical and the numerical values, their comparison showed a 0%.

Table 5.6: Ratio of The Analytical and The Numerical Values of σ_1 Along F-X1A's Shear Span

Height Coordinate from c.o.g. (mm)	Length Coordinate (mm)						
	304.8	558.8	812.8	1066.8	1320.8	1524.0	
-228.60	115.89%	0.00%	0.00%	0.00%	0.00%	0.00%	
-101.60	-1325.92%	108.62%	95.25%	99.91%	148.58%	0.00%	
-88.90	-839.04%	110.32%	95.53%	99.63%	147.19%	0.00%	
-76.20	-602.40%	111.80%	95.83%	99.36%	145.55%	0.00%	
-63.50	-461.84%	113.06%	96.13%	99.12%	143.66%	0.00%	
-50.80	-368.36%	114.11%	96.45%	98.88%	141.55%	-0.01%	
-38.10	-301.47%	114.96%	96.77%	98.66%	139.28%	-0.01%	
-25.40	-251.03%	115.62%	97.10%	98.44%	136.90%	-0.01%	
-12.70	-211.48%	116.11%	97.42%	98.23%	134.45%	-0.01%	ana./
0.00 Neutral Axis	-179.51%	116.44%	97.75%	98.03%	131.97%	-0.02%	num.
12.70	-153.03%	116.64%	98.07%	97.82%	129.49%	-0.03%	
25.40	-130.69%	116.72%	98.38%	97.62%	127.02%	-0.06%	
38.10	-111.58%	116.69%	98.69%	97.41%	124.59%	-0.18%	
50.80	-95.08%	116.60%	98.99%	97.21%	122.21%	0.39%	
63.50	-80.78%	116.45%	99.28%	97.00%	119.87%	0.15%	
76.20	-68.37%	116.29%	99.56%	96.79%	117.58%	0.17%	
88.90	-57.65%	116.13%	99.82%	96.58%	115.34%	2.23%	
101.60	-48.48%	116.02%	100.06%	96.37%	113.14%	47.25%	
228.60	0.00%	0.00%	0.00%	91.11%	90.64%	99.44%	

5.3. Re-imagination of The Diagonal Cracks

One last step before the size effect study could commence is the re-imagination of the shear tension crack. In this step, the author simply redrew the actual shear tension crack, such as the one pictured in Figure 5.1, on the mirror images of the specimens which were created in one of the steps of the data rearrangement explained in subchapter 5.1.3. The goal for doing this step is to find the σ_1 values along the crack for further analyses.

An example of the redrawn shear tension crack is presented in Figure 5.11. In this example, the shear tension crack from the F-X1A specimen was copied to its mirror image by selecting every cell that was located at the coordinates of the crack, which was then marked with a red color. To obtain the σ_1 values more conveniently, the crack was drawn as a straight line instead of following the actual propagation path of the shear tension crack. This simplification was allowed to be done since the actual crack itself almost formed a linear line that had just some minor deviations on specific points of the crack, and also because the finite element models of the specimens had a relatively fine element size.
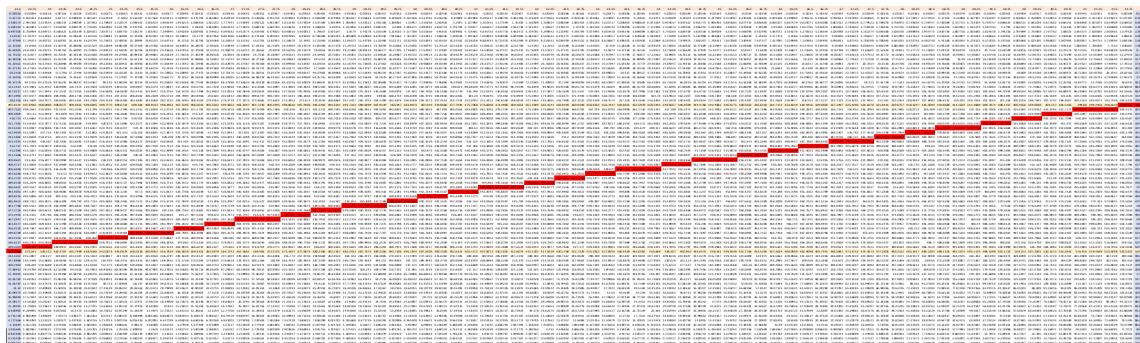
Figure 5.11: Redrawn Shear Tension Crack on The Mirror Image of F-X1A
Specimen

5.4. Size Effect Investigation and Its Results

After all numerical analyses and data rearrangements on the selected specimens of Hanson's were complete, the data was ready to be used for studying the structural size dependency of the uniaxial tensile strength. To narrow the scope of the study, the investigation into the size effect was focused only on the web part of the specimens where the shear tension cracks occurred. The σ_1 area approach, which was explained in Chapter 4, was utilized to assist the author in detecting the size effect and its results are described in the following subchapters.

In addition to the numerical results from Hanson's selected beams, other results from another report were added into the pool of data to sharpen the outcome of the study. They were the numerical results from the Elzanaty's and the Choulli's specimens which were produced by Kroeze (2018) using LEFEA for his own study on shear tension cracks. Similar to Hanson's, these additional numerical results were also processed through the data rearrangement and reimagination-of-the-shear-tension-crack processes for the purpose of obtaining the σ_1 values along their shear tension cracks.

Unfortunately, after further observation, several selected specimens of Hanson's were deemed to be unfit to be included in the analyses because it was found that the stress distribution in the specimens with flexural cracks could not be predicted accurately when analyzed using the LEFEA. The error in the stress distribution of the specimens with flexural cracks was evident when the maximum principal tensile stress from the whole web was compared to the maximum principal tensile stress from a shear crack $(\sigma_{1max,wholeweb}/\sigma_{1max,crack})$, as shown in Table 5.7. The comparison showed that $\sigma_{1max,wholeweb}/\sigma_{1max,crack}$ ratios were consistently larger than one, while the $\sigma_{1max,wholeweb}$ located at the bottom web-flange junction of the specimens, except for F-1A and F-1B specimens. These results from Table 5.7 gave an indication that the shear tension cracks on Hanson's specimens with flexural cracks should have initiated from the bottom web-flange junction of the specimens instead from the actual location where the shear tension cracks occurred as reported by Hanson in his dissertation.

This inaccuracy of LEFEA result in specimens with flexural cracks was mentioned in the study by Kroeze (2018) in which he assumed that it was caused by the presence of the flexural cracks. The error can possibly be explained by the force redistribution when the flexural cracks appeared which formed a new force equilibrium and also by the tension softening that the specimens might experience at the location of $\sigma_{1max,wholeweb}$ which cannot be predicted by the LEFEA. As a side note, the $\sigma_{1max,crack}$ values for F-1A and F-1B were not exactly located at the crack because the shear tension cracks were assumed as a linear crack on the mirror images, but its differences with $\sigma_{1max,crack}$ values were negligible. For further references, σ_{1max} is referred to $\sigma_{1max,crack}$.

Because of this issue with Hanson's selected specimens, only the data collected from F-1A and F-1B was kept in the data pool. They are kept together with the other data originated from the Elzanaty's and Choulli's specimens and put together into a list of 'trusted' specimens presented in Table 5.8.

Table 5.7: $\sigma_{1max,crack}$, $\sigma_{1max,wholeweb}$, Their Ratio, and $\sigma_{1max,wholeweb}$ Location

	Specimen	$\sigma_{1max,crack}$ (MPa)	$\sigma_{1max,wholeweb}$ (MPa)	$\sigma_{1max,wholeweb}$ / $\sigma_{1max,crack}$	**Location of** $\sigma_{1max,wholeweb}$
Hanson	F-X1A	3.08	4.02	1.31	Bottom W-F Junction
	F-X1B	2.59	3.61	1.39	Bottom W-F Junction
	F-1A	3.37	3.38	1.00	Near The Middle of STC
	F-1B	3.51	3.51	1.00	Near The Middle of STC
	F-2A	3.70	4.49	1.21	Bottom W-F Junction
	F-2B	3.14	3.57	1.14	Bottom W-F Junction
	F-3A	3.63	3.75	1.03	Bottom W-F Junction
	F-3B	2.86	3.10	1.08	Bottom W-F Junction
	F-4B	3.33	4.63	1.39	Bottom W-F Junction
	F-5A	2.81	3.86	1.37	Bottom W-F Junction
	F-5B	3.36	3.86	1.15	Bottom W-F Junction
	F-19A	3.33	3.82	1.15	Bottom W-F Junction

note: W-F = Web-Flange
STC = Shear Tension Crack

Table 5.8: List of The Trusted Specimens

Hanson	**Elzanaty**	**Choulli**
F-1A	CW1	HAP1E
F-1B	CW8	HAP2E
		HAP1W
		HAP2W
		HAP1TE
		HCP2TW

5.4.1. Investigation into The Size Effect Using σ_1 Area Approach

In this section, the steps for obtaining the results from the application of σ_1 area approach on all trusted specimens are described. The results are presented in the form of a graph that plot the relation between the areas of the σ_1 rectangles and the values of normalized maximum principal tensile stress (σ_{1max}/f_{ctm}) from the shear tension cracks of the trusted specimens. The σ_{1max}/f_{ctm} values, in particular, shows how close the maximum principal tensile stress was to the mean uniaxial tensile strength when a shear tension crack occurred. The relation between these two variables was then used to determine if the structural size can have an effect on the f_{ctm} values and causes a premature shear tension cracking.

Firstly, in order to obtain the areas of the σ_1 rectangles, plots between σ_1 values along a shear tension crack of each trusted specimen vs. the crack length were created in combination with a constant line of reduced maximum principal tensile stress value $(\sigma_{1max,red.})$. The plot of σ_1 values vs. the crack length is shown as a curvy blue line and the $\sigma_{1max,red.}$ constant line is shown as a grey line, as shown in Figure 5.12 as an example. The other similar graphs from other trusted specimens can be found at Appendix A. The curvy blue line and the grey line were then created two intersection points which produced a length that was later multiplied with the thickness of the web to form the σ_1 rectangle, as illustrated in Figure 4.1. Additionally, a line

of a constant f_{ctm} value was also added to each of these graphs as an upper bound limit to the plot of σ_1 values. The purpose of this line is to show the repetitive occurrence of shear tension cracking on the trusted specimens that happened at a principal tensile stress level that was lower than the designated uniaxial tensile strength of the specimens.
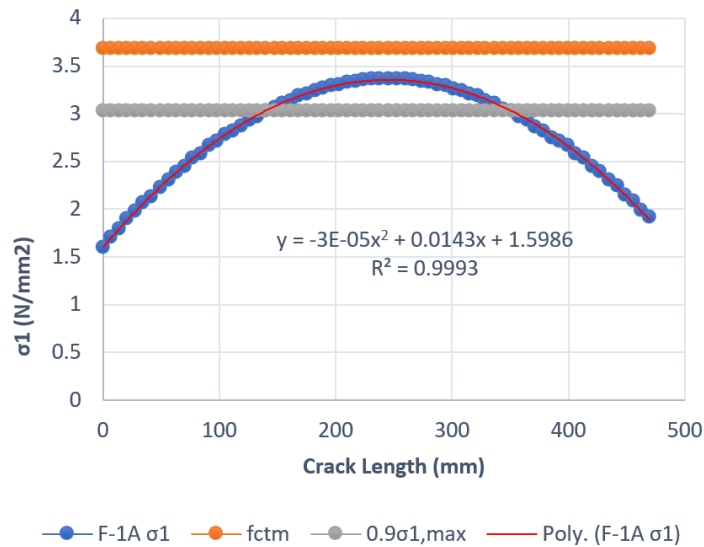
Figure 5.12: σ_1 Along The Crack vs. The Crack Length of F-1A Specimen

Next, after the rectangles areas were found, a plot between the areas of the σ_1 rectangles and σ_{1max}/f_{ctm}, shown in Figure 5.13, was created. In this plot, it appears that the data points were concentrating at two different ranges of areas: one is at around 10,000 mm^2 to 20,000 mm^2 where the data points of Elzanaty's and Hanson's are located and the other is at around 50,000 mm^2 to 60,000 mm^2 where Choulli's data points are. The data of σ_{1max}, σ_{1max}/f_{ctm}, and σ_1 rectangles areas used for generating this plot is presented in Table 5.9.
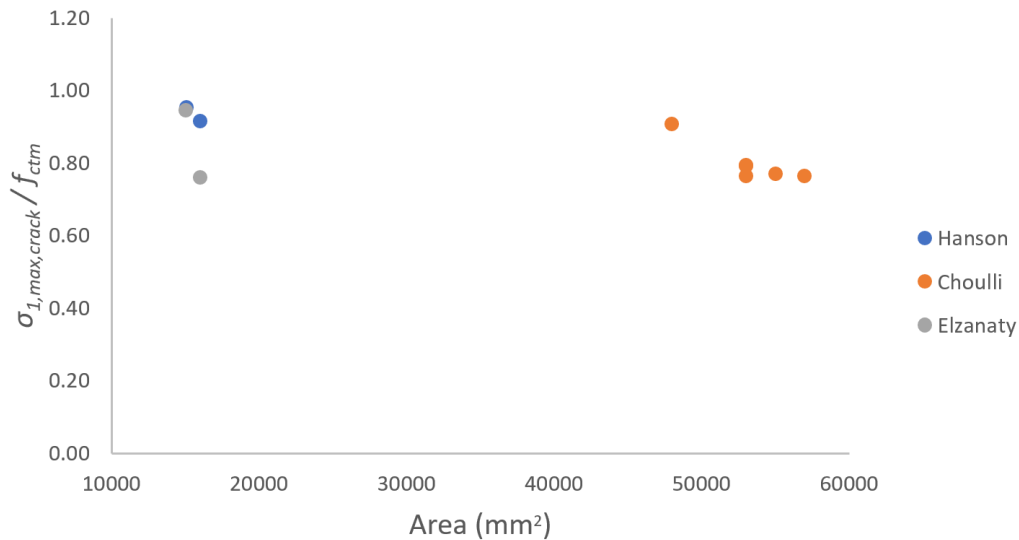
Figure 5.13: σ_{1max}/f_{ctm} vs. The σ_1 Rectangles Areas with Trusted Specimens
(in SI units)

Table 5.9: Values of σ_{1max}, σ_{1max}/f_{ctm}, and σ_1 Rectangles Areas

	Specimen	σ_{1max} (MPa)	σ_{1max}/f_{ctm} (MPa)	σ_1 Area (mm^2)
Hanson	F-1A	3.37	0.91	16040.06
	F-1B	3.51	0.95	15112.86
Elzanaty	CW1	4.33	0.95	15000.00
	CW8	2.56	0.76	16000.00
Choulli	HAP1E	4.03	0.80	53000.00
	HAP2E	3.87	0.77	55000.00
	HAP1W	3.88	0.76	53000.00
	HAP2W	3.84	0.77	57000.00
	HAP1TE	3.89	0.79	53000.00
	HCP2TW	4.44	0.91	48000.00

Lastly, in the same plot, a trendline was generated to show the relationship between the two variables of the plot based on the available data points, as shown in Figure 5.14. A linear trendline was chosen after all other types of trendline because it had the largest coefficient of determination (R^2) value at 0.4213 indicating that this trendline had the best fit for this data set. In the plot area, it appears that the trendline had a negative slope, which means that the value of σ_{1max}/f_{ctm} tend to decrease with the increase of the σ_1 rectangle area. A mathematical equation that represents the linear relation between the two variables is $y = -3 \times 10^{-6}x + 0.9409$.
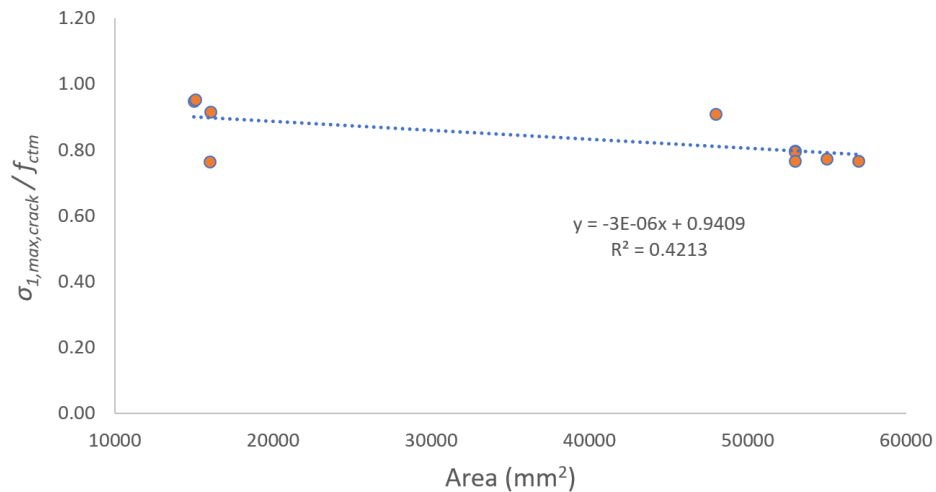
Figure 5.14: Trendline of σ_{1max}/f_{ctm} vs. The σ_1 Rectangles Areas Plot (in SI units)

5.4.2. Investigation into The Size Effect using Ratio-of-Distances Approach

A description of how the ratio-of-distances approach produced its results was presented in this section. Similar to the σ_1 area method, the result of this method is also given in the form of a graph that shows a relationship between the volumes of the web part of the trusted specimens and the ratio of distances $(\ell_{\sigma_{1max}}/\ell_{c.o.g.})$. In ratio of distances, $\ell_{\sigma_{1max}}$ is the vertical distance from σ_{1max} location to the web-flange junction and $\ell_{c.o.g.}$

is the vertical distance from the same web-flange junction to the beam's neutral axis.

To begin with, the values of $\ell_{\sigma_{1max}}$, $\ell_{c.o.g.}$, and the web-part volumes needed to be defined. The web-part volumes were calculated using the web width, the web length, and the shear span of each trusted specimen as reported by Hanson, Elzanaty, and Choulli in their theses. On the other hand, $\ell_{\sigma_{1max}}$ and $\ell_{c.o.g.}$ were defined straightforwardly by having their length measured in the mirror images of the trusted specimens. The defined values of $\ell_{\sigma_{1max}}$, $\ell_{c.o.g.}$, and the web-part volumes and their related information for each trusted specimen are given in Table 5.10.

Table 5.10: $\ell_{\sigma_{1max}}/\ell_{c.o.g.}$, Web-Part Volumes, and Their Related Information for Each Trusted Specimen

	Specimen	$\ell_{\sigma1max}/\ell_{c.o.g.}$	Web Height (mm)	Web Width (mm)	Shear Span (mm)	Web-Part Volume (m³)
Hanson	F-1A	0.94	203.20	76.20	762.00	11799
	F-1B	1.00	203.20	76.20	762.00	11799
Elzanaty	CW1	0.87	228.60	50.80	1070.00	12426
	CW8	0.78	228.60	50.80	1384.00	16072
Choulli	HAP1E	0.99	370.00	100.00	2347.50	86858
	HAP2E	0.49	370.00	100.00	2250.00	83250
	HAP1W	0.87	370.00	100.00	2347.50	86858
	HAP2W	0.74	370.00	100.00	2250.00	83250
	HAP1TE	0.86	370.00	100.00	2347.50	86858
	HCP2TW	0.99	370.00	100.00	2250.00	83250

After all data was collected, the graph of $\ell_{\sigma_{1max}}/\ell_{c.o.g.}$ vs. web-part volume was produced, as shown in Figure 5.15. In the plot area, it is clear that there is a relatively large distance between Hanson's and Elzanaty's data points and Choulli's data points in the axis of web-part volume. It indicates that the group of Hansons's and Elzanaty's trusted specimens are comparatively much smaller in size than the group of Choulli's. Nevertheless, it appears that both groups have a similar spread of data points in the axis of $\ell_{\sigma_{1max}}/\ell_{c.o.g.}$ at values around 0.74 to 1, except for HAP2E which had $\ell_{\sigma_{1max}}/\ell_{c.o.g.}$ value of 0.49.
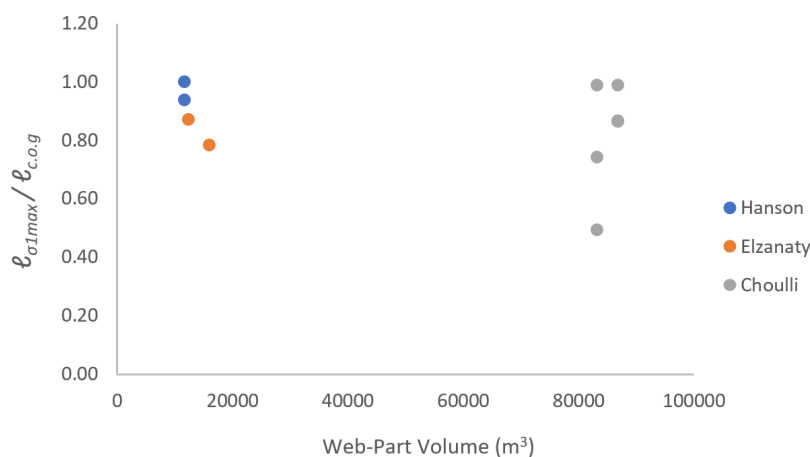
Figure 5.15: $\ell_{\sigma_{1max}}/\ell_{c.o.g.}$ vs. The Web-Part Volume with Trusted Specimens (in SI units)

5.5. Discussion

The result obtained from the σ_1 area approach provides some hints that indicate the size effect played a significant role in premature shear tension cracking on the web of the trusted specimens. Firstly, a hint was given by how the data points of Hanson's and Elzanaty's are more concentrated on the range of σ_{1max}/f_{ctm} level that is closer to 1 than the data points of Choulli's. Hanson's and Elzanaty's had σ_{1max} levels at around 90-95% of their f_{ctm}, except for CW8, and Choulli's had σ_1 levels that were a bit lower than 80% of their f_{ctm}, except for HCP2TW. If the two outliers are neglected, these results show a clear proof that the tensile strength of the concrete structure is size dependent.

Secondly, another hint can also be found from the linear trendline of σ_1 area method result. The effect was revealed by the negative slope of the linear trendline that represents the declining relation between σ_{1max}/f_{ctm} and σ_1 rectangles areas. This trendline proves that, even by including the two outliers, there is a trend of declining tensile strength with the increase of structural size. The trend is shown by the location of the data point on the trendline where Hanson's and the Elzanaty's data points, which represent the smaller specimens, are located at the higher left side of the trendline and the Choulli's, which represent the larger specimens, are located at the lower right side of the trendline.

Unfortunately, the reliability of the linear trendline chosen for the result of σ_1 area approach suffered from the lack of data. The trendline shows low reliability by having a relatively low value of R^2 despite being the best fit for the data sets of the approach. This issue can be easily resolved by adding more data that comes from similar specimens into the analyses to increase the R^2 value closer to 1.

In contrast, the result of the ratio-of-distances approach seems to give no indication of the presence of the size effect. It shows that the data points of Hanson's and Elzanaty's has a similar spread along the axis of $\ell_{\sigma_{1max}}/\ell_{c.o.g.}$ to the data points of Choulli's, except for the data point of HAP2E which had $\ell_{\sigma_{1max}}/\ell_{c.o.g.}$ value of 0.49. When the outlier of HAP2E was removed, it was obvious that the shear cracks from the smaller specimens and the shear cracks from the larger specimens had a similar starting points locations, at which the σ_{1max} was located. This means that, even though the Hanson's and Elzanaty's webs were much smaller in volume than Choulli's, their shear cracks initiated at similar distance ratios. Thus, it can be concluded that the structural size does not give any influence to the location of σ_{1max} and this approach cannot be used for detecting size effect in shear tension cracking.

Moreover, according to the results, it is obvious that the area around the neutral axis of the beam is more vulnerable to shear tension cracking than the area around the web-flange junction of the trusted specimens. The vulnerability is again shown through the values of $\ell_{\sigma_{1max}}/\ell_{c.o.g.}$ of the trusted specimens which showed that most of the shear cracks started from near the neutral axis $\left(\ell_{\sigma_{1max}}/\ell_{c.o.g.} = 0.74 - 1.00\right)$, except for HAP2E that had a shear tension crack that started closer to the web-flange junction $\left(\ell_{\sigma_{1max}}/\ell_{c.o.g.} = 0.49\right)$. This result gave a sign that the resistance of the web against shear tension cracking is possibly higher around the web-flange junction than around the beam neutral axis, which agrees with the base assumption of the ratio-of-distances approach.

In addition, these results also verify the capability of the two new approaches to identifying the size effect in shear tension cracking. In this case, it appears that the σ_1 area approach is more reliable than the ratio-of-distances approach in finding the size dependency of the uniaxial tensile strength. The σ_1 area approach was able to show the presence of size effect on the trusted specimens while the ratio-of-distances method was not. It seems that the reason is that the assumption used for the latter approach is not correct because the location of σ_{1max} is not governed by the size of the structure. Thus, for a future attempt on studying the size effect in shear tension cracking, the author suggests the use of the σ_1 area approach over the ratio-of-distances approach.

6

Conclusion and Recommendation

6.1. Conclusion

This thesis had an objective of verifying the concrete uniaxial tensile strength dependency on structural size in its relation with the premature shear tension cracking on the web of prestressed concrete beams. For this purpose, a group of several I-profiled prestressed concrete beams experimented by Hanson (1964), Choulli (2005), and Elzanaty (1986), named the trusted specimens, were numerically investigated using linear elastic finite element analysis (LEFEA) to generate the true principal tensile stress distributions at the occurrence of shear tension cracking. The principal tensile stress along the crack of each specimen was observed using two new approaches proposed by the author in an attempt to detect the presence of the size effect. These two approaches are the σ_1 area approach and the ratio-of-distances approach.

The results of the research that answer the given research questions are briefly described below:

1. *Is there any presence of size effect regarding the resistance of prestressed concrete beams on shear tension cracking?*

   The σ_1 area approach presented a result that confirmed the presence of size effect in shear tension cracking at the trusted specimens. The confirmation was given by how the data points of Hanson's and Elzanaty's were widely separated from the Choulli's at the axis of the area of the rectangles while having higher σ_{1max}/f_{ctm} values than the Choulli's. This condition showed that there was a tendency for the smaller specimens to have a higher resistance towards shear tension cracking compared to the larger specimens, which gave a clear indication to the presence of the size effect. Alternatively, the evidence of the size dependency was also found in the negative slope of the linear trendline that gave the declining relation between σ_{1max}/f_{ctm} and the rectangles areas. This relation described a trend of the larger specimens having resistance against tensile stress that is lower than its designated strength.

   On the contrary, the ratio-of-distances approach did not manage to detect the size effect in shear tension cracking on the trusted specimens. The result of this approach implied that the shear cracks from the smaller specimens and the shear cracks from the larger specimens had a similar starting points locations, at which the σ_{1max} was located. This means that, even though the Hanson's and Elzanaty's webs were much smaller in volume than Choulli's, their shear cracks initiated at similar distance ratios. Consequently, it is evident that the structural size does not give any influence to the starting location of the shear tension cracks and the ratio-of-distances approach cannot be relied on detecting the size effect.

2. *Is the resistance of the shear tension crack at the web-flange junction higher than anywhere in the web?*

   The result of the ratio-of-distances approach indicated that the area around the neutral axis of the trusted specimens is more susceptible to shear tension cracking than the area around the web-flange junction. The susceptibility is shown through the values of $\ell_{\sigma_{1max}}/\ell_{c.o.g.}$ of the trusted specimens which showed that most of the shear cracks started from near the neutral axis, except for HAP2E. This

43

result was considered as a sign that the resistance of web towards shear tension cracking is possibly higher around the web-flange junction than around the beam neutral axis, which agrees with the base assumption of the ratio-of-distances approach.

Also, these results also verify the capability of the proposed approaches in identifying the size effect in shear tension cracking. In this case, it appears that the σ_1 area approach is more reliable than the ratio-of-distances approach in finding the size dependency of the uniaxial tensile strength. The σ_1 area approach was able to show the presence of size effect on the trusted specimens while the ratio-of-distances method was not. It seems that the reason is that the assumption used for the latter approach is not correct because the location of $\sigma_{1\,max}$ is not governed by the size of the structure. Thus, for a future attempt on studying the size effect in shear tension cracking, the author suggests the use of the σ_1 area approach over the ratio-of-distances approach.

6.2. Recommendation

For future research related to the work in this thesis, the author recommended the following research topics:

Nonlinear Finite Element Analysis on Specimens with Flexural Cracks near the Shear Tension Cracks

One of the limitations for observing the size effect in this thesis is the presence of flexural cracks near the shear tension cracks. Their presence rendered the principal tensile stress distribution generated by the LEFEA to be inaccurate since there must be force redistribution from the concrete to the reinforcements when the flexural cracks formed. It is recommended for the coming study to use the nonlinear finite element analysis for obtaining the true principal tensile stress distribution along the crack to be used for detecting the size effect.

Size Effect on Specimens under Uniformly Distributed Load

Studying the early formation of shear tension crack on the web of prestressed concrete beams under the influence of uniformly distributed load is another interesting case to be investigated. An investigation on this case will give a new relation that describes the influence of structural size on the reduction of tensile strength on larger size concrete structures.

Bibliography

[1] British Standard Institution. *Eurocode 2: design of concrete structures: British standard*. London: BSi, 2008.

[2] Youssef Choulli. *Shear behavior of prestressed I-beams made with high-strength self compacting concrete*. PhD thesis, Universitat Politecnica De Catalunya, 2005.

[3] Michael P. Collins and Denis Mitchell. *Prestressed Concrete Structures*. Prentice Hall, Englewood Cliffs, 1990.

[4] Ashraf H. Elzanaty. *Shear critical high-strength concrete beams*. PhD thesis, Cornell University, 1985.

[5] Slate F.O. Elzanaty A.H., Nilson A.H. Shear capacity of prestressed concrete beams using high-strength concrete. *ACI Journal Proceedings*, (77):359–368, 1986. ISSN 0002-8061. doi: 10.14359/10436.

[6] John M Hanson. *Ultimate shear strength of prestressed concrete beams with web reinforcement*. PhD thesis, Lehigh University, 1964.

[7] Russell C. Hibbeler. *Mechanics of Materials*. Pearson Prentice Hall, 8 edition, 2011. ISBN 9780136022305.

[8] Sijtse Jan Kroeze. *Resistance to diagonal tension cracking in prestressed beams*. PhD thesis, Delft University of Technology, 2018.

[9] S. Timoshenko and J.N. Goodier. *Theory of Elasticity*. McGraw-Hill, 2 edition, 1951.

[10] Joost C. Walraven. Background document for prENV 1992-1-1:2002. Technical report, 2002.

[11] Hans Welleman and Coen Hartsuijker. Introduction into Continuum Mechanics. *CT4145/CT2031 Mechanics of Structures Lecture Note TU Delft*, 1(April):76, 2008.

Appendices

A
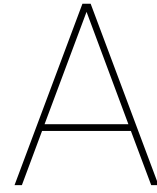
Data and Graphs of Hanson's, Choulli's, and Elzanaty's Selected Specimens

A.1. Result from Hanson's
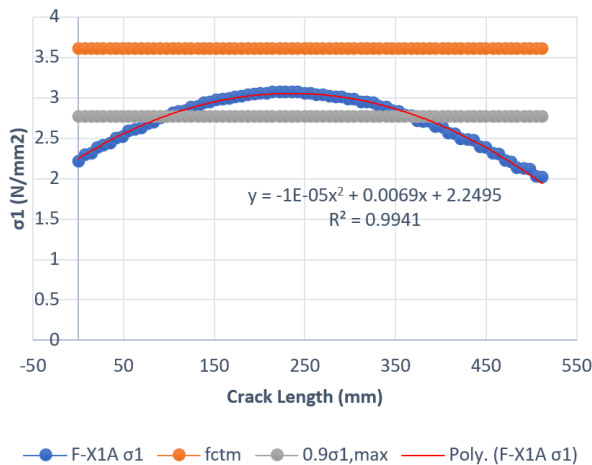
Maximum σ_1 value at shear tension crack	3.08	MPa
f_{ctm} capacity used	85.06%	
Distance between the intersection points	280.94	mm
σ_1 rectangle area	21407.87	mm^2
$\ell\sigma_{1max}$	88.90	mm
$\ell_{c.o.g.}$	101.60	mm
$\ell\sigma_{1max} / \ell_{c.o.g.}$	87.50%	

Figure A.1: σ_1 Along The Crack vs. The Crack Length of F-X1A and Other Information
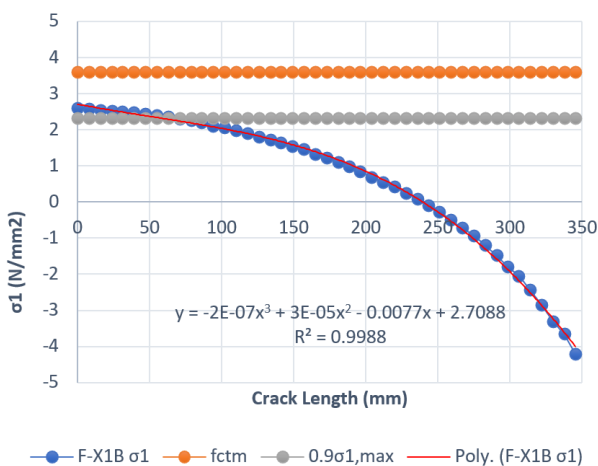
Maximum σ_1 value at shear tension crack	2.59	MPa
f_{ctm} capacity used	71.61%	
Distance between the intersection points	56.49	mm
σ_1 rectangle area	4304.29	mm^2
$\ell\sigma_{1max}$	0.00	mm
$\ell_{c.o.g.}$	101.60	mm
$\ell\sigma_{1max} / \ell_{c.o.g.}$	0.00%	

Figure A.2: σ_1 Along The Crack vs. The Crack Length of F-X1B and Other Information

49
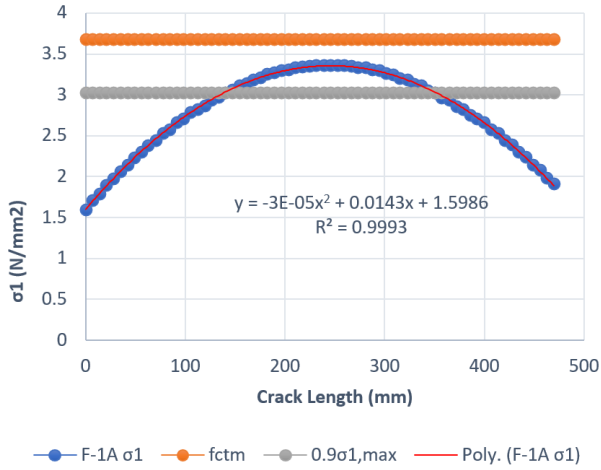
Maximum σ_1 value at shear tension crack	3.37	MPa
f_{ctm} capacity used	91.51%	
Distance between the intersection points	210.50	mm
σ_1 rectangle area	16040.06	mm^2
$\ell\sigma_{1max}$	95.25	mm
$\ell_{c.o.g.}$	101.60	mm
$\ell\sigma_{1max} / \ell_{c.o.g.}$	93.75%	

Figure A.3: σ_1 Along The Crack vs. The Crack Length of F-1A and Other Information
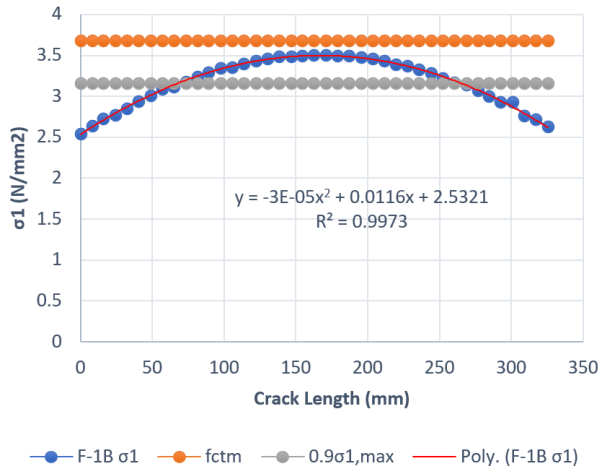
Maximum σ_1 value at shear tension crack	3.51	MPa
f_{ctm} capacity used	95.21%	
Distance between the intersection points	198.33	mm
σ_1 rectangle area	15112.86	mm^2
$\ell\sigma_{1max}$	101.60	mm
$\ell_{c.o.g.}$	101.60	mm
$\ell\sigma_{1max} / \ell_{c.o.g.}$	100.00%	

Figure A.4: σ_1 Along The Crack vs. The Crack Length of F-1B and Other Information
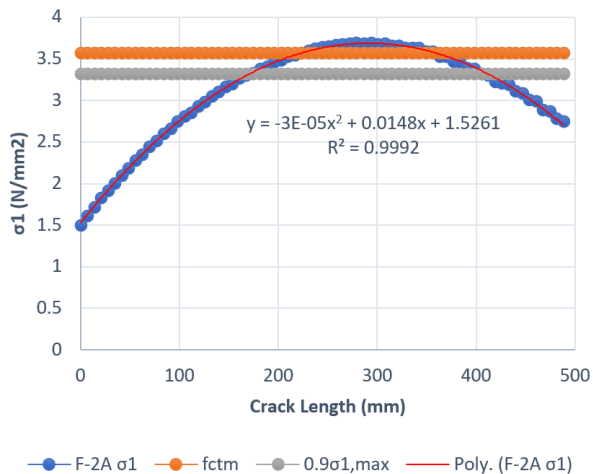
Maximum σ_1 value at shear tension crack	3.70	MPa
f_{ctm} capacity used	103.33%	
Distance between the intersection points	238.77	mm
σ_1 rectangle area	18194.60	mm^2
$\ell\sigma_{1max}$	82.55	mm
$\ell_{c.o.g.}$	101.60	mm
$\ell\sigma_{1max} / \ell_{c.o.g.}$	81.25%	

Figure A.5: σ_1 Along The Crack vs. The Crack Length of F-2A and Other Information
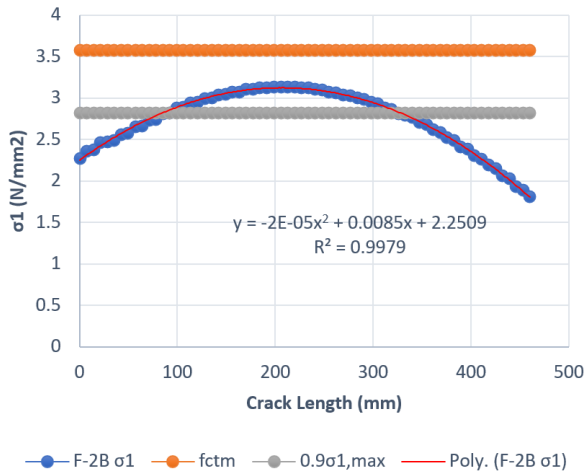
Maximum σ_1 value at shear tension crack	3.14	MPa
f_{ctm} capacity used	87.79%	
Distance between the intersection points	241.66	mm
σ_1 rectangle area	18414.23	mm²
$\ell\sigma_{1max}$	95.25	mm
$\ell_{c.o.g.}$	101.60	mm
$\ell\sigma_{1max} / \ell_{c.o.g.}$	93.75%	

Figure A.6: σ_1 Along The Crack vs. The Crack Length of F-2B and Other Information
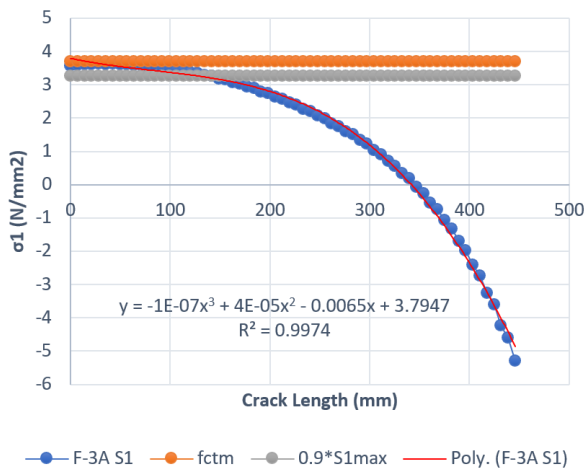
Maximum σ_1 value at shear tension crack	3.63	MPa
f_{ctm} capacity used	98.21%	
Distance between the intersection points	128.86	mm
σ_1 rectangle area	9819.10	mm²
$\ell\sigma_{1max}$	19.05	mm
$\ell_{c.o.g.}$	101.60	mm
$\ell\sigma_{1max} / \ell_{c.o.g.}$	18.75%	

Figure A.7: σ_1 Along The Crack vs. The Crack Length of F-3A and Other Information
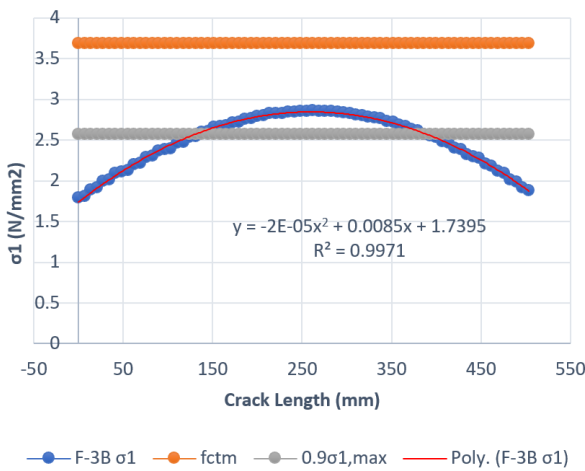
Maximum σ_1 value at shear tension crack	2.86	MPa
f_{ctm} capacity used	77.53%	
Distance between the intersection points	257.09	mm
σ_1 rectangle area	19589.90	mm²
$\ell\sigma_{1max}$	95.25	mm
$\ell_{c.o.g.}$	101.60	mm
$\ell\sigma_{1max} / \ell_{c.o.g.}$	93.75%	

Figure A.8: σ_1 Along The Crack vs. The Crack Length of F-3B and Other Information

$$y = -2E-05x^2 + 0.0087x + 2.0998$$
$$R^2 = 0.9928$$

Maximum σ_1 value at shear tension crack	3.33	MPa
f_{ctm} capacity used	95.39%	
Distance between the intersection points	279.77	mm
σ_1 rectangle area	21318.39	mm^2
$\ell\sigma_{1max}$	88.90	mm
$\ell_{c.o.g.}$	101.60	mm
$\ell\sigma_{1max} / \ell_{c.o.g.}$	87.50%	
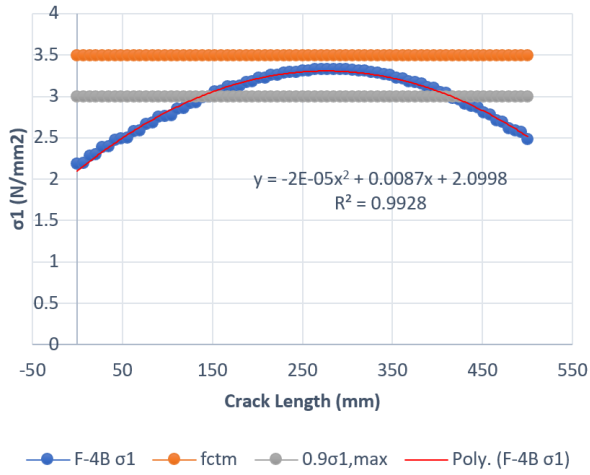
Figure A.9: σ_1 Along The Crack vs. The Crack Length of F-4B and Other Information

$$y = -2E-05x^2 + 0.0106x + 1.183$$
$$R^2 = 0.9967$$

Maximum σ_1 value at shear tension crack	2.81	MPa
f_{ctm} capacity used	79.88%	
Distance between the intersection points	257.12	mm
σ_1 rectangle area	19592.63	mm^2
$\ell\sigma_{1max}$	88.90	mm
$\ell_{c.o.g.}$	101.60	mm
$\ell\sigma_{1max} / \ell_{c.o.g.}$	87.50%	
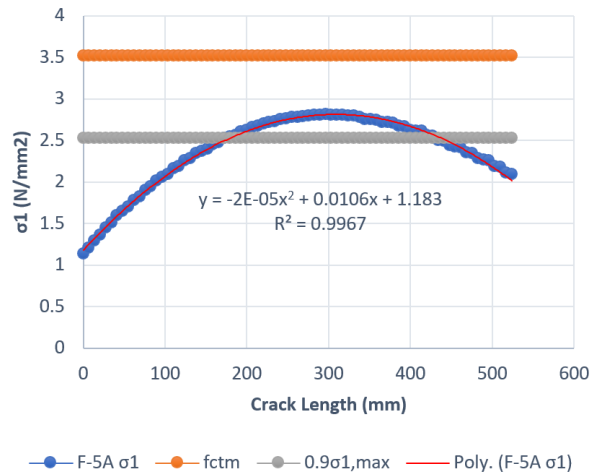
Figure A.10: σ_1 Along The Crack vs. The Crack Length of F-5A and Other Information

$$y = -2E-05x^2 + 0.0182x - 0.3466$$
$$R^2 = 0.9986$$

Maximum σ_1 value at shear tension crack	3.36	MPa
f_{ctm} capacity used	95.45%	
Distance between the intersection points	164.41	mm
σ_1 rectangle area	12528.28	mm^2
$\ell\sigma_{1max}$	19.05	mm
$\ell_{c.o.g.}$	101.60	mm
$\ell\sigma_{1max} / \ell_{c.o.g.}$	18.75%	
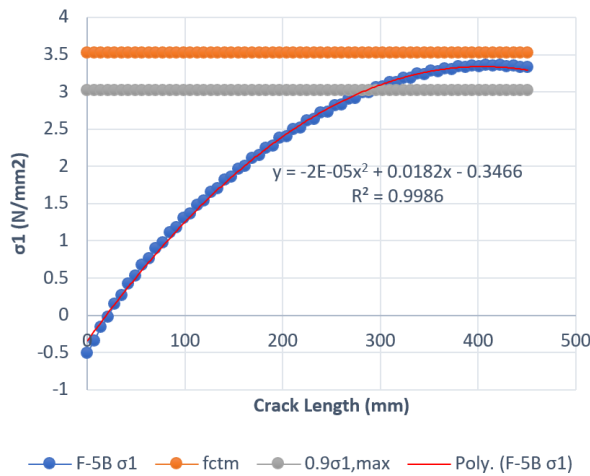
Figure A.11: σ_1 Along The Crack vs. The Crack Length of F-5B and Other Information

Figure and table:

$y = 1E\text{-}08x^3 - 3E\text{-}05x^2 + 0.0162x + 0.9226$
$R^2 = 0.9993$
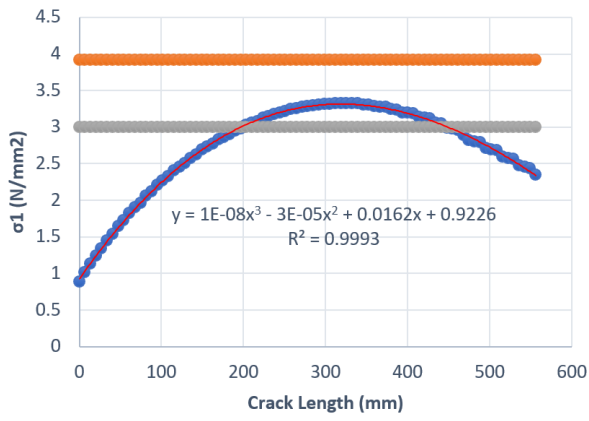
Maximum σ_1 value at shear tension crack	3.33	MPa
f_{ctm} capacity used	85.02%	
Distance between the intersection points	261.17	mm
σ_1 rectangle area	19900.86	mm^2
$\ell_{\sigma_{1max}}$	95.25	mm
$\ell_{c.o.g.}$	101.60	mm
$\ell_{\sigma_{1max}} / \ell_{c.o.g.}$	93.75%	

Figure A.12: σ_1 Along The Crack vs. The Crack Length of F-19A and Other Information

A.2. Result from Choulli's
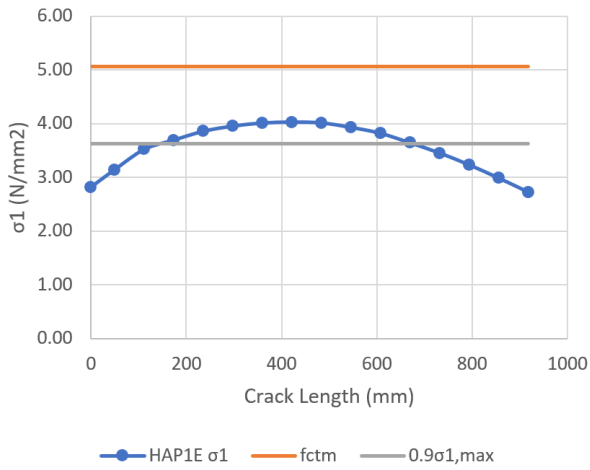
Maximum σ_1 value at shear tension crack	4.03	MPa
f_{ctm} capacity used	79.62%	
Distance between the intersection points	530.00	mm
σ_1 rectangle area	53000.00	mm^2
$\ell\sigma_{1max}$	200.00	mm
$\ell_{c.o.g.}$	202.59	mm
$\ell\sigma_{1max} / \ell_{c.o.g.}$	98.72%	

Figure A.13: σ_1 Along The Crack vs. The Crack Length of HAP1E and Other Information
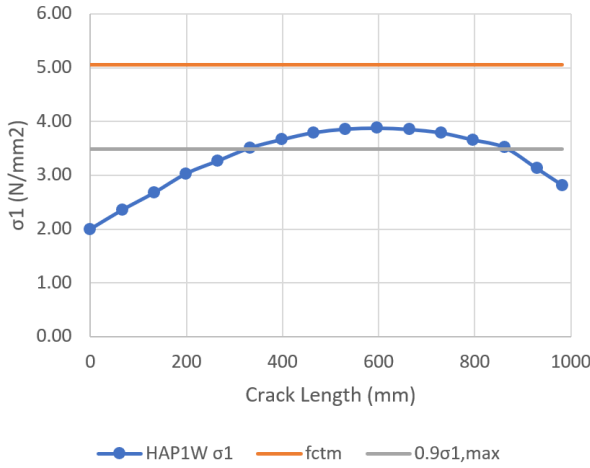
Maximum σ_1 value at shear tension crack	3.88	MPa
f_{ctm} capacity used	76.60%	
Distance between the intersection points	530.00	mm
σ_1 rectangle area	53000.00	mm^2
$\ell\sigma_{1max}$	145.00	mm
$\ell_{c.o.g.}$	167.41	mm
$\ell\sigma_{1max} / \ell_{c.o.g.}$	86.61%	

Figure A.14: σ_1 Along The Crack vs. The Crack Length of HAP1W and Other Information

Figure A.15: σ_1 Along The Crack vs. The Crack Length of HAP2E and Other Information
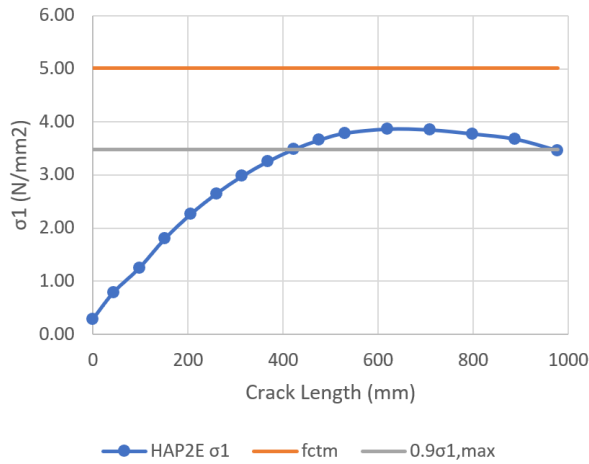
Maximum σ_1 value at shear tension crack	3.87	MPa
f_{ctm} capacity used	77.25%	
Distance between the intersection points	550.00	mm
σ_1 rectangle area	55000.00	mm^2
$\ell\sigma_{1max}$	100.00	mm
$\ell_{c.o.g.}$	202.59	mm
$\ell\sigma_{1max} / \ell_{c.o.g.}$	49.36%	

Figure A.16: σ_1 Along The Crack vs. The Crack Length of HAP2W and Other Information
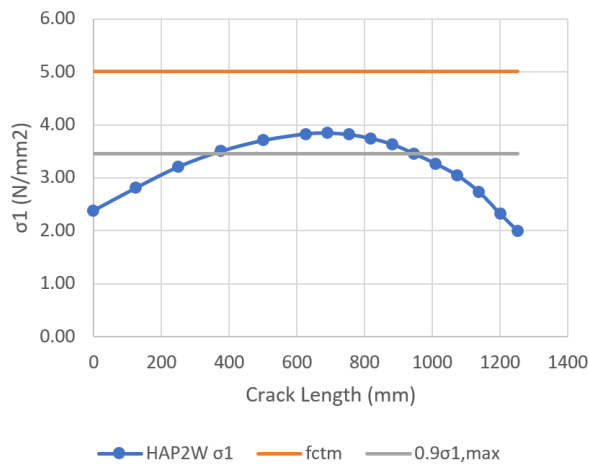
Maximum σ_1 value at shear tension crack	3.84	MPa
f_{ctm} capacity used	76.62%	
Distance between the intersection points	570.00	mm
σ_1 rectangle area	57000.00	mm^2
$\ell\sigma_{1max}$	150.00	mm
$\ell_{c.o.g.}$	202.59	mm
$\ell\sigma_{1max} / \ell_{c.o.g.}$	74.04%	

Figure A.17: σ_1 Along The Crack vs. The Crack Length of HAP1TE and Other Information
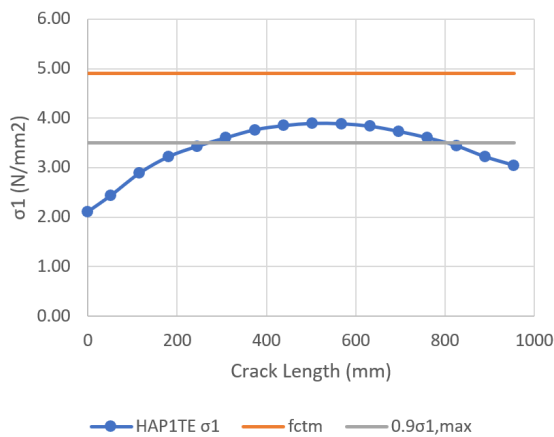
Maximum σ_1 value at shear tension crack	3.89	MPa
f_{ctm} capacity used	79.42%	
Distance between the intersection points	530.00	mm
σ_1 rectangle area	53000.00	mm^2
$\ell\sigma_{1max}$	175.00	mm
$\ell_{c.o.g.}$	202.59	mm
$\ell\sigma_{1max} / \ell_{c.o.g.}$	86.38%	

Maximum σ_1 value at shear tension crack	4.44	MPa
f_{ctm} capacity used	90.94%	
Distance between the intersection points	480.00	mm
σ_1 rectangle area	48000.00	mm^2
$\ell\sigma_{1max}$	200.00	mm
$\ell_{c.o.g.}$	202.59	mm
$\ell\sigma_{1max} / \ell_{c.o.g.}$	98.72%	
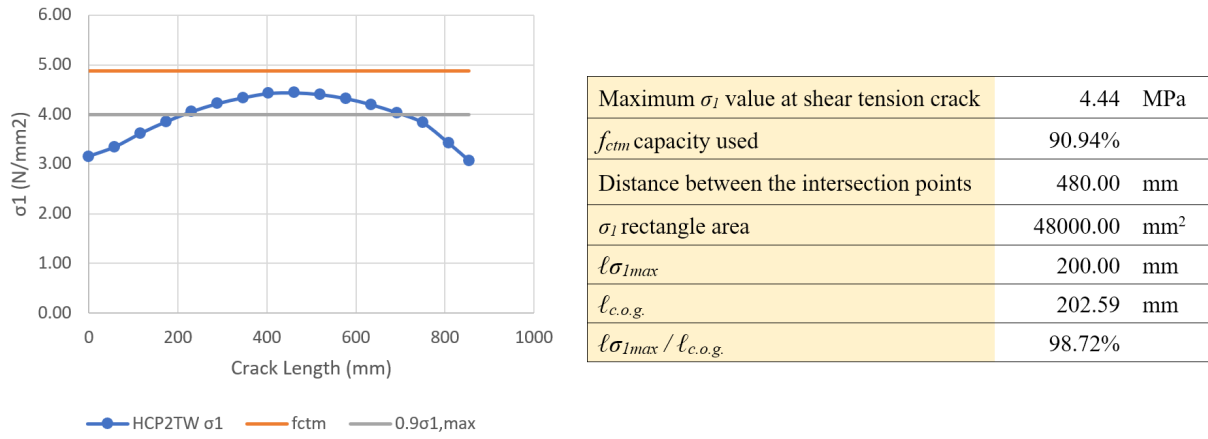
Figure A.18: σ_1 Along The Crack vs. The Crack Length of HCP2TW and Other Information

A.3. Result from Elzanaty's
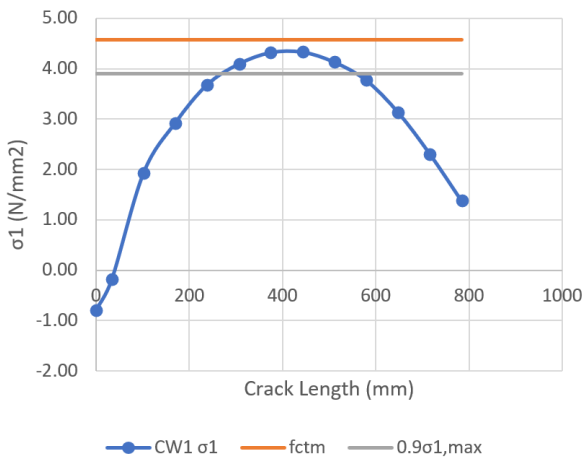
Maximum σ_1 value at shear tension crack	4.33	MPa
f_{ctm} capacity used	94.57%	
Distance between the intersection points	290.00	mm
σ_1 rectangle area	15000.00	mm^2
$\ell\sigma_{1max}$	100.00	mm
$\ell_{c.o.g.}$	115.00	mm
$\ell\sigma_{1max} / \ell_{c.o.g.}$	86.96%	

Figure A.19: σ_1 Along The Crack vs. The Crack Length of CW1 and Other Information
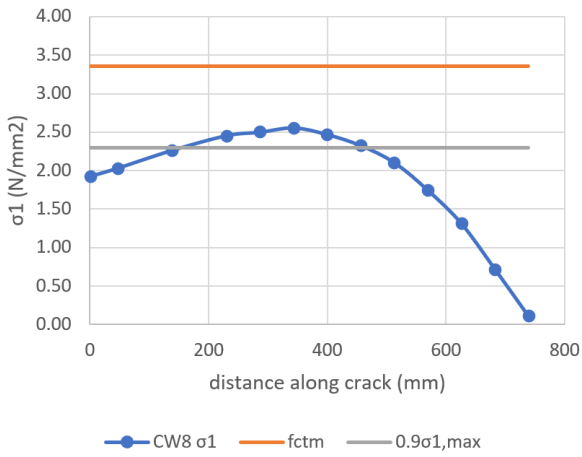
Maximum σ_1 value at shear tension crack	2.56	MPa
f_{ctm} capacity used	76.25%	
Distance between the intersection points	310.00	mm
σ_1 rectangle area	16000.00	mm^2
$\ell\sigma_{1max}$	90.00	mm
$\ell_{c.o.g.}$	115.00	mm
$\ell\sigma_{1max} / \ell_{c.o.g.}$	78.26%	

Figure A.20: σ_1 Along The Crack vs. The Crack Length of CW8 and Other Information

B

Python Script for Data Rearrangement

In [ ]:

```python
import numpy as np
import matplotlib.pyplot as plt
import pandas as pd
import xlsxwriter
from collections import import OrderedDict
%matplotlib inline
beam_case = 'F-19A' # change beam name here
```

In [ ]:

```python
file = beam_case+'_ps_raw.xlsx'
xl = pd.ExcelFile(file)
```

In [ ]:

```python
df1 = xl.parse('NEAT') #calling the data from tab 'NEAT'
```

In [ ]:

```python
print (df1)
```

In [ ]:

```python
x = np.array(df1.X) # storing X data in an array called x
y = np.array(df1.Y) # storing Y data in an array called y
elid = np.array(df1.EL_ID) # storing EL_ID data in an array called elid
z = np.array(df1.S1) # storing S1 data in an array called z
z1 = np.array(df1.S2) # storing S2 data in an array called z1
```

In [ ]:

```python
y2 = np.array(df1.Y)
y2.sort()
print(y2)
```

In [ ]:

```python
y3 = list(OrderedDict.fromkeys(y2)) # list of Y coordinate in order (duplicate removed)
y3_as = np.asarray(y3)
y3_l = y3_as.tolist()
y3_l.insert(39,4.875)
y3_l.insert(105,13.125)
y3_as = np.asarray(y3_l)
y3 = y3_as
print(y3)
print(len(y3))
```

In [ ]:

```python
y4 = y3[-1::-2] # list of Y coordinate in reverse order in step of 2
#y4[19] = y3[0]
y5 = y4[-1::-1] # list of Y coordinate in order
print(y4)
print(len(y4))
print(y5)
print(len(y5))
```

In [ ]:

```python
x2 = np.array(df1.X)
x2.sort() # list of sorted x coordinate
print(x2)
```

In [ ]:

```python
x3 = list(OrderedDict.fromkeys(x2)) # list of sorted x coordinate (duplicate removed)
x4 = x3[::2]
print(x3)
print(len(x3))
print(x4)
print(len(x4))
```

In [ ]:

```python
qw = np.zeros((len(y4), len(x4))) # zero matrix to store S1 data
qw2 = np.zeros((len(y4), len(x4))) # zero matrix to store data of numbers of S1 data per co
qw3 = np.ones((len(y4), len(x4)))
qw5 = np.zeros((len(y4), len(x4)))
qw6 = np.zeros((len(y4), len(x4)))
```

In [ ]:

```python
qwsyy = np.zeros((len(y4), len(x4))) # zero matrix to store S2 data
qw2syy = np.zeros((len(y4), len(x4))) # zero matrix to store data of numbers of S2 data per
qw3syy = np.ones((len(y4), len(x4)))
qw5syy = np.zeros((len(y4), len(x4)))
```

In [ ]:

```python
for i in range(len(y4)):
    for j in range(len(x4)):
        for k in range(len(x)):
            if y5[i] == y[k]:
                if x4[j] == x[k]:
                    qw[i,j] += z[k] # storing S1 data at qw matrix
                    qw2[i,j] +=1 # counting S1 data per coordinate
                    qwsyy[i,j] += z1[k] # storing S2 data at qw matrix
                    qw2syy[i,j] +=1 # counting S2 data per coordinate


#step for doing manual nodal averaging
```

In [ ]:

```python
workbook = xlsxwriter.Workbook(beam_case+'_ps_raw(OUT_CNode).xlsx')
worksheet = workbook.add_worksheet('S1')
```

In [ ]:

```python
row = 0
col = 0
row1 = 1
col1 = 1
```

In [ ]:

```python
for Y in (y4): # writing the sorted, duplicate-free Y coordinate on Excel tab S1
    worksheet.write(row1, col, Y)
    row1 += 1
```

In [ ]:

```python
for X in (x4): # writing the sorted, duplicate-free Y coordinate on Excel tab S1
    worksheet.write(row, col1, X)
    col1 += 1
```

In [ ]:

```python
for q in range(len(y4)):
    for r in range(len(x4)):
        if qw2[q,r] >=1:
            qw3[q,r] = qw2[q,r] # to replace or the zero in qw2 matrix with 1 for division
```

In [ ]:

```python
print (qw3)
```

In [ ]:

```python
qw4 = (qw/qw3) # nodal averaging
print (qw4)
plt.imshow(qw4, interpolation='nearest')
plt.colorbar()
```

In [ ]:

```python
for t in range(len(y4)):
    qw5[len(y4)-1-t,:] = qw4[t,:] # storing nodal averaging data at qw4 in reverse order (i
    #to mimic the stress distribution of the model at DIANA
```

In [ ]:

```python
for o in range(len(y4)):
    for p in range(len(x4)):
        worksheet.write(o+1, p+1, qw5[o,p]) # write the qw5 data at Excel
```

In [ ]:

```python
print (qw5)
plt.imshow(qw5, interpolation='nearest')
plt.colorbar()
```

In [ ]:

```python
worksheet2 = workbook.add_worksheet('S2')
```

In [ ]:

```python
row = 0
col = 0
row1 = 1
col1 = 1
```

In [ ]:

```python
for Y in (y4): # writing the sorted, duplicate-free Y coordinate on Excel
    worksheet2.write(row1, col, Y)
    row1 += 1
```

In [ ]:

```python
for X in (x4): # writing the sorted, duplicate-free X coordinate on Excel
    worksheet2.write(row, col1, X)
    col1 += 1
```

In [ ]:

```python
for q in range(len(y4)): # writing the sorted, duplicate-free X coordinate on Excel
    for r in range(len(x4)):
        if qw2syy[q,r] >=1:
            qw3syy[q,r] = qw2syy[q,r]
```

In [ ]:

```python
print (qw3syy)
```

In [ ]:

```python
qw4syy = (qwsyy/qw3syy)
print (qw4syy)
plt.imshow(qw4syy, interpolation='nearest')
plt.colorbar()
```

In [ ]:

```python
for t in range(len(y4)):
    qw5syy[len(y4)-1-t,:] = qw4syy[t,:] # storing nodal averaging data at qw4 in reverse or
```

In [ ]:

```python
for o in range(len(y4)):
    for p in range(len(x4)):
        worksheet2.write(o+1, p+1, qw5syy[o,p]) # write the qw5syy data at Excel
```

In [ ]:

```python
print (qw5syy)
plt.imshow(qw5syy, interpolation='nearest')
plt.colorbar()
```

In [ ]:

```python
worksheet3 = workbook.add_worksheet('node_num')

for l in range(len(y4)):
    qw6[len(y4)-1-l,:] = qw2[l,:]

for g in range(len(y4)):
    for h in range(len(x4)):
        worksheet3.write(g+1, h+1, qw6[g,h])
```

In [ ]:

```python
workbook.close()
```